TERAHERTZ REFLECTION TIME-DOMAIN SPECTROSCOPY FOR IMAGING AND IDENTIFYING CONCEALED INTERFACES IN MULTILAYERED SYSTEMS

by

Seth Lowry

B.Sc., University of Northern British Columbia, 2017

THESIS SUBMITTED IN PARTIAL FULFILLMENT OF
THE REQUIREMENTS FOR THE DEGREE OF
MASTER OF SCIENCE
IN
PHYSICS

UNIVERSITY OF NORTHERN BRITISH COLUMBIA

August 2020

Abstract

This thesis reviews multiple forms of terahertz spectroscopy and imaging, and exploits a combination of aspects from the techniques involved to undertake a novel method. With the use of this method, subsurface interfaces within a practical, insulated system are spatially imaged and identified. Initially, transmission spectroscopy is used to select the insulating material of the system based on favourable dielectric properties, followed by the use of dove prism reflection spectroscopy to understand and qualitatively contrast the responses of the interfaces to reflecting terahertz pulses. After constructing a reflection imaging system, multiple interface materials concealed by insulation are successfully located and identified by coloured overlays in a 100 by 100 image. Further exploration of applications involving the proposed method is also discussed.

TABLE OF CONTENTS

LIST OF TABLES

LIST OF FIGURES

LIST OF ABBREVIATIONS

LIST OF CONTRIBUTIONS

Journal Articles

[A1] B. D. Price, S. N. Lowry, I. D. Hartley, and M. Reid, "Subterahertz refractive flat-top beam shaping via 3D printed aspheric lens combination," *Applied Optics*, vol. 59, no. 18, pp. 5429-5436, 2020.

[A2] E. Lozowski, M. R. A. Shegelski, M. Hawse, S. N. Lowry, C. Sample, and M. Reid, "Comment on 'A Scratch-Guide Model for the Motion of a Curling Rock'," *Tribology Letters*, vol. 68, no. 2, 2020.

Conference Presentations

[C1] S. N. Lowry and M. Reid, "Terahertz Reflection Imaging for Concealed Interface Inspection [PowerPoint Presentation]," *UNBC Interdisciplinary Weekly Seminar Series*, Prince George, BC, Canada. October 2019.

[C2] B. D. Price, S. N. Lowry, and M. Reid, "THz refractive top-hat beam shaping via 3D-printed aspheric lens combination," *Poster presented at the 2018 Canadian Undergraduate Physics Conference*, Edmonton, AB, Canada. August 2018.

[C3] B. D. Price, S. N. Lowry, I. D. Hartley, and M. Reid, "THz Michelson Interferometer for measuring properties of engineered wood products,", *Poster presented at the 2017 Canadian Undergraduate Physics Conference*, Ottawa, ON, Canada. October 2017.

[C4] S. N. Lowry, P. Kilcullen, and M. Reid, "Towards a Digital Micro-Mirror Array-based, Broadband Single Pixel Camera," *Poster presented at the 2016 Canadian Undergraduate Physics Conference*, Halifax, NS, Canada. October 2016.

Acknowledgements

I am delighted to extend my sincere thanks towards those who have made this project possible. Foremost, I cannot begin to express my thanks to my supervisors, Dr. Matthew Reid and Dr. Mark Shegelski. It is with their patient guidance, knowledge and genuine support that has given me the chance to not only become the researcher I am, but to profoundly enjoy my first few years of research. I am deeply indebted to Dr. Reid for providing me with research opportunities in a novel field for many years throughout my education, introducing me to exciting projects to be a part of, and managing my first visit to the east coast to share my research at a conference. I am also extremely grateful to Dr. Shegelski for allowing me to gain experience and confidence giving lectures in numerous physics courses, and especially for the continuous, valuable advice and support over the years. They are the key reasons why my passion for physics is so great, in regards to both research and teaching.

Particularly helpful to me during the beginning of my studies was my third committee member, Dr. Alex Aravind, who encouraged stimulating conversations regarding the generalities of research, as well as Dr. Ian Hartley and his vast supply of interesting questions and ideas towards a project. I would also like to thank everyone from the Physics Department at UNBC and those at the Wood Innovations Research Lab for their interest in assisting in this project.

Finally, I must express my deepest appreciation and gratitude for my friends and family who have never wavered in their support, specifically throughout the duration of this project. My utmost appreciation goes to my parents, who have always pushed me to excel in my passions and interests and have never stopped believing in me, to my sister, who has never failed to help through the more difficult times, and to Sophie for her endless patience and friendship through all of the ups and downs of my research. I want to also extend my thanks to friends and family I did not mention, who have consistently shown interest in my work and research.

Introduction

Recent advancements in terahertz (THz) technology have led to innovations in imaging, spectroscopy, and non-destructive evaluation (NDE) techniques. This stable access to a new frequency range of light has led to cutting-edge advancements and diversified strategies in this field of research. Measuring the interaction between matter and differing frequencies of light allows for characterizations of that material; this is classified as a form of spectroscopy. For NDE purposes, measuring the reflectance of light from matter can be a useful form of spectroscopy, which is called reflection spectroscopy. This allows interfaces of differing materials to be examined and evaluated.

The purpose of this thesis is to review important contributions made in the field of imaging, NDE, and reflection spectroscopy at THz frequencies of light to determine the most appropriate implementation for conducting concealed interface inspection. Further, this work realizes such an implementation and exploits it to demonstrate an example of subsurface interface imaging appropriate for NDE. The scope includes analyzing current NDE techniques that implement THz reflection spectroscopy for imaging, quality assessment, and characterization of materials and interfaces, identifying limits in current NDE techniques where THz imaging may present a feasible alternative, and demonstrates a functional system suitable for further work to expand NDE methods in THz technology.

Outline of this Thesis

Chapter 1 contains a brief overview of the history of THz radiation as well as its involvement in various forms of spectroscopy. THz applications are explored from research in controlled environments to applied, practical systems in industry. A comparison of techniques from each area is undertaken to set the stage for the project of this thesis.

Chapter 2 details a common mechanism for the generation and detection of pulsed THz radiation, as well as its operation in THz time-domain spectroscopy (THz-TDS). Two theoretical models regarding different forms of spectroscopy for the extraction of material dielectric properties are also developed.

Chapter 3 reports the experimental methods involved in transmission and reflection spectroscopy, as well as the implementation of a reflection imaging system for the identification of subsurface interfaces within an insulated system. A collection of images are displayed based on various amplitude and phase characteristics of the reflected THz pulses. Interface-specific image filters are described and applied to a reflection image, successfully locating and identifying each interface material.

Chapter 4 conclusively summarizes the experimental results of this thesis, and emphasizes its importance to broadening the use of THz in NDE, followed by suggestions for future direction.

Chapter 1

Terahertz Imaging & Spectroscopy

1.1 Terahertz Radiation

Terahertz (THz) radiation, sometimes referred to as far-infrared radiation or submillimeter waves, corresponds to a frequency range of the electromagnetic spectrum between microwaves and the infrared range of light [1]. Inherent from the prefix *tera* (T), these frequencies usually exist upwards to approximately 3 THz (10^{12} Hz) and can reach as low as 300 GHz (10^{9} Hz). Until recent technological advancements, the stable production of electromagnetic waves in this range of frequencies has been difficult to access in a compact setting [2]. For many years, the electromagnetic frequencies produced by conventional electronic methods have not extended up to terahertz frequencies, nor have they been accessible by optical methods involving lasers and semiconductors [3]. The frequency roll-off from these common methods creates a gap in the electromagnetic spectrum, commonly referred to as the 'THz gap.' This technological impasse poses a substantial practical challenge for the production of radiation in this range of frequencies, and also serves to define the characteristic range of frequencies in the THz region.

The rising interest in exploring THz frequencies over the years has been driven by this phenomenon, and has given rise to novel methods since the 1970's for the stable production and coherent detection of THz radiation by borrowing concepts from both optical and electronic domains. Following this technological leap, significant progress has been made in improving THz technology, thus increasing the accessibility of frequencies within the THz gap. Now, with a growing expanse of experimental methods and diverse production of THz equipment, the regular conduction of THz research in a compact setting is no longer a challenging task. Recent applications of THz science span many areas of non-destructive evaluation (NDE) [4], food inspection [5], security screening [6], art preservation [7], medicine [8], as well as imaging [9].

THz radiation retains numerous appealing qualities regarding its interactions with some materials. These unique properties are driving the pursuit for new applications in the constantly evolving THz field. THz radiation propagates through a vast selection of dry, non-conducting materials, such as plastics, foams, and composites, with minimal absorption, motivating a range of applications towards the quality testing of packaged materials and detection of corrosion under insulation [10]. With applications heavily involved in NDE techniques, competition between THz and the previously prominent X-ray technology naturally exists. In applications for which the use of THz technology is applicable, it has proven to excel due, in part, to the inherent safety of using this type of radiation since THz frequencies are non-ionizing and do not have the required photon energy to directly damage DNA structures within a biological system, as opposed to X-rays [11]. The sub-millimetre wavelength provides sufficient resolution for many imaging applications, and demonstrates unique interactions upon reflection with water [12, 13]. These qualities are limited by the heavy absorption of THz frequencies in atmospheric moisture, restricting propagation distances to tens of meters, which is still suitable for many applications.

With innovation in technology, the methods of producing and detecting THz radiation have diversified over the years, lending different varieties of THz sources for a given application. Common continuous-wave (*cw*) THz sources take advantage of photomixing two laser modes of a different frequency of light in order to produce a monochromatic THz beam at the difference frequency [14]. These lasers exhibit a high power density for a given frequency, but are limited in bandwidth and solely rely on intensity-based measurements. These *cw* sources are often adapted to specific applications for NDE in industry. With the rapid commercialization of femtosecond (fs) laser sources in the early 1990's, the development of *ultrafast* THz systems has enabled the coherent detection of THz pulses [15]. In these systems, femtosecond laser pulses interact with an emitter, releasing a range of THz frequencies in a pulse. The bandwidth of these pulses consists of frequencies as low as 0.1 THz up to 5 THz. The femtosecond laser is also used to gate the receiver, which allows for direct time-domain mapping of the electric field on a sub-picosecond (ps) time scale. Even though compact sources and detectors for THz frequencies are readily available for a laboratory setting, research in THz technology continues to discover more cost-efficient systems and designs.

1.2 Applications of THz Radiation for NDE

Since the advancements in electronics and photonics that led to the access of the THz gap, there have been numerous applications for THz imaging. These range from moisture content and concealed object imaging in biological materials [16,17], to absorption spectroscopy for the identification of drugs/explosives [18], to security screening applications [11], and finally to the detection of flaws in materials within insulated systems such as submarine hulls [19] and the NASA space shuttle foam insulation [20]. Imaging with THz can be performed in a transmission or reflection geometry, each of these methods specialized for certain applications based on their respective strengths and weaknesses. Transmission imaging with THz provides information regarding the full complex dielectric function (index of refraction and absorption coefficient) of a sample, whereas reflection imaging can provide unique surface and interface information which may be difficult or even impossible to obtain via transmission.

For example, the complex dielectric characteristics of liquid water and other polar liquids cannot be extracted by the use of transmission spectroscopy, due to the heavy absorption of THz radiation by polar liquids [21]. By containing a liquid water sample below a silicon window, the multiply reflected THz pulse (at the surface of the window, and the silicon-water interface) contains amplitude and phase information of the electric field of the reflected THz pulse. Analysis of the effects of liquid water on these measured quantities allows the determination of the dielectric properties of the sample.

One of the important aspects of these configurations is the delay line that enables THz time-domain spectroscopy (THz-TDS). This allows each delayed pulse to be paired with its associated reference pulse, in order to determine the relative time delay of the pulse travelling through the sample. There are many characteristic changes in pulse shape and position of the THz pulse in the time-domain that are used to determine the properties of the sample transmitted through or reflected from. Transmission imaging is generally used in materials in which THz radiation will propagate in order to detect the pulse on the opposite side of the sample. Reflection imaging is often used in multilayered systems where propagation through the sample is not possible, and this technique becomes extremely effective with concealed objects/interfaces that are highly reflective. Examples utilizing transmission imaging are the imaging of food products low in water content [17], the imaging of water content in a leaf [22], automobile dashboard inspection of the foam padding between plastic parts [1], and security screening for weapons, drugs or explosives [23, 24]. By taking measurements with a pulsed THz spectrometer through chocolate bars contaminated with glass splinters, small stones, and screws, Jördens and Koch find sudden intensity drops in the transmitted pulse used to determine the presence of these contaminants [17]. An image of the contaminated chocolate bar still in its original packaging is produced, identifying the intrusive objects. A small stone embedded in the chocolate bar is identified by a drop in transmitted intensity from the image scan due to increased scattering or absorption of the THz pulse. This report demonstrates the ability of THz-TDS imaging to detect foreign bodies in chocolate bars and suggests the applicability of THz imaging to food products in low moisture environments.

THz transmission spectroscopy can also be applied to the detection of illicit drugs and explosives. Due to the specific structure of the chemicals involved in drugs and explosives, the absorption spectra in the THz range for different materials can vary significantly. Reports from Kawase et al. and Kemp conclude that the identification of drugs and explosives with THz transmission spectroscopy is possible, even when these powders are concealed by materials transparent to THz frequencies, such as envelopes and cloth [18, 23]. By measuring the absorption spectra for methylenedioxymethamphetamine (MDMA), aspirin and other methamphetamines separately, these drugs are detectable within an envelope packaging, and a spatial image is produced, visually classifying each substance. It can be noticed that absorption peaks at certain frequencies are very distinguishable for a given material. In many materials that interact minimally with THz radiation, the absorption curve increases with frequency, and peaks along the absorption curve can be specific to certain substances. A similar technique is used to identify explosive powders such as Semtex, trinitrotoluene (TNT), and Royal Demolition eXplosive (RDX), also known as cyclonite [18]. Taking security applications further, recent progress has been made by moving towards merging microwave and THz imaging for security screening in airports [6]. The high resolution of THz radiation and the lesser absorption in the atmosphere of microwaves allows for the detection of metallic objects concealed underneath clothing.

Mittleman et al. exercise the use of a THz-TDS system for the identification of various individual gases as well as gas mixtures [25]. Absorption lines at specific frequencies illustrate absorption fingerprints that are used for gas identification. Closely related gases are also distinguished by exploiting the time delay of THz pulse ”commensurate” echoes to examine characteristic rotational energies.

Applications for reflection spectroscopy and imaging at THz frequencies expand into the field of NDE of manufactured materials. In many manufactured products, errors often occur in mouldings, sealant, and insulation, and over time these materials can wear down. With NDE techniques, these flaws and defects can be located without removal of insulation or destruction of the product. For some reflection spectroscopy applications, the lack of the ability to perform transmission spectroscopy makes the identification of concealed objects by their optical properties difficult since absorption spectra, or absorption ’fingerprints’, may not be present in reflections. It is also complicated by the fact that a well-defined reference, required for spectroscopy, is not always possible to collect. THz-TDS reflection imaging is involved in art conservation [7], under paint corrosion detection [26], and concealed interface inspection such as foam insulation defect detection in the NASA space shuttle [20] and void detection in submarine acoustic tiles [19]. Fukunaga and Picollo demonstrate the impact that THz reflection spectroscopy could have on art conservation [7]. Although they find that the interaction between THz radiation and many art materials is difficult to model, they demonstrate the impact this form of imaging can have on art conservation and restoration processes. A THz-TDS reflection image of a painting is generated which identifies gold foil and lead paint used on the panel by the reflectance of each material. The materials involved in each layer of the painting are also identified based on the time delay and intensity of the THz pulse, essentially quantifying the materials in terms of their corresponding reflections. Reflections from an interface at a further depth correlate to a measurement at a later time delay due to its increased time-of-flight, indicating the depth position of that interface. The addition of a wooden structural enforcement on the back of the painting is also identified in this manner. By performing THz spectroscopy with numerous art materials, identification of paints, binders, and other art materials can be utilized for restoration purposes.

Taking THz-TDS imaging for NDE further, a field of interest is discovering hidden areas of corrosion or damage in metals and composites. Anastasi and Madaras investigate the detection of corrosion underneath varying thicknesses of paint [26]. This report relies on the changes in paint thickness and shape as a result of corrosion of the underlying metal. When the painted metal corrodes, the paint can swell and take on a rough shape. This changes the optical path and reflectance, thus affecting the detected time delay of the signal. It is found that when the paint layer becomes thin, the surface reflections become indistinguishable as the time delays of the reflected pulses from the surfaces of the paint and metal approach a common value. Nonetheless, chips and holes are detected with certainty, while corrosion detection may require further signal processing methods. These methods are utilized in THz reflection spectroscopy, discussed further in Section 1.3.

Numerous reports have studied the evaluation of damaged high strength composites involved in lightweight aircraft manufacturing. Stoik et al. report on the identification of voids, delaminations, paint removal and damage on layered composite systems important for aircraft production [27]. For multi-layered systems, where multiple back-reflections are expected from the layered system composed of various media, the reflection from the interface remains consistent if the dielectric contrast between the two media (i.e. sample-air) is consistent throughout the scanned sample. Changes in the amplitude or phase of the interface reflection provides information on how the interface has changed. Stoik et al. identify how this reflection changes with delaminations, damage and burns at an interface [27]. Detecting these flaws in manufactured composites before use in aircraft is of vital importance to the quality and structure of the aircraft.

In a similar apparatus, NDE for foam insulation and shuttle tiles on the NASA space shuttle has shown to be suitable with THz frequencies. Anastasi et al. compare the THz reflection images of corroded aluminum with the same sample concealed by the shuttle tiles [20]. It is concluded that the newfound ability to detect corrosion in a layered system from access to only one side of the sample is more difficult to detect with shuttle tiles that absorb heavily at THz frequencies. Two images are produced of the corroded region from spatial plots of the peak-to-peak value of the THz pulse and of the amplitude of a chosen frequency. Similar images have previously been produced for inspecting voids in the foam insulation in the NASA space shuttle as well.

Kilcullen et al. produce reflection images for the detection of water-filled voids between acoustic tiles surrounding the hull of a submarine [19]. The strong reflection from the rubber-water interface is relied on to locate the presence of water before corrosion can occur. Similar to the shuttle tiles, the acoustic tiles heavily absorb THz radiation, and make it difficult to gather a detectable back-reflection. It suggests that for any system in which the layered sample has a small dielectric contrast among the media, regions of high dielectric contrast can be used for detection of water or metals.

What all of these examples have in common is that reflection imaging is not amenable to reflection <u>spectroscopic</u> imaging because a well defined reference pulse has not been available or has been impossible to achieve. In this thesis, we identify, construct and demonstrate a system that can be used to identify materials at a concealed interface by exploiting the spectrum of reflected THz pulses.

1.3 Reflection Spectroscopy in the Lab

There are numerous industrial applications of spectroscopic testing and NDE using THz radiation, and with state-of-the-art technology allowing the use of new electromagnetic frequencies in the THz range, there are many applications for THz reflection spectroscopy and the collection of dielectric properties of materials. By measuring the electric field of reflected THz pulses in the time-domain with a THz-TDS system, the Fourier-transformed data provides access to both amplitude (used traditionally in reflection imaging) and phase information (which is exploited in this work) to determine dielectric properties for the purpose of identifying materials at a concealed interface. These material-specific functions are expected as the THz pulses respond in reflection to the underlying dielectric function $\tilde{\epsilon}(\omega)$, complex index of refraction $\tilde{n}(\omega) = \sqrt{\tilde{\epsilon}(\omega)}$ and absorption coefficient $\alpha(\omega)$ [28]. In order to work with amplitude and phase information most effectively, a reference reflection measurement must be performed without the sample in the THz-TDS system, as well as a sample reflection measurement. The ratio of the two measurements transformed into the frequency domain is used to determine amplitude and phase shifts required for comparison to calculations. Results of this kind have been published for various dielectric materials, therefore calculating dielectric properties allows the probed sample to be identified. The ability of identifying materials in the lab setting is simplified by close-range detection and controlled humidity for minimally disturbed THz pulses, as opposed to the real environment required for most applications [29]. For this reason, most reflection imaging at THz frequencies has exploited amplitude-only information. Where the phase is also used to study full dielectric functions, a well-defined reference is used. In this work, the gap between lab-based reflection spectroscopy and practical industrial imaging is tackled with promising initial results.

Lab-based reflection spectroscopy shares the same principles as spectroscopy in transmission mode, discussed briefly in Section 1.2. The key difference is that position-sensitive measurements now pose a challenge since any change in position of the sample introduces a change in time-of-flight of the pulse and an associated change in phase. To avoid this, a fixed window can be introduced to hold the sample without affecting the point of reflection. Thrane et al. introduce a reflection spectroscopy technique for the extraction of dielectric properties of highly absorbing liquids such as liquid water, performing index of refraction and absorption coefficient measurements [30]. In agreement with previous theoretical models, THz reflection spectroscopy also shows that water molecules can change orientation while maintaining hydrogen bonds. Uhd Jepsen and Fischer present the quantification of the dynamic range of the absorption coefficient detected for dielectric materials [31]. It is concluded that by using reflection spectroscopy, as opposed to transmission spectroscopy, larger absorption coefficients can be more reliably measured. It has been noticed that higher frequencies of spectrometers are less dependable in transmission modes for absorption peaks, whereas reflection modes are limited mostly by laser fluctuations.

In summary, there are some key points to be outlined regarding two perspectives of reflection spectroscopy. In the case of lab-based experiments for which the determination of dielectric properties of liquids, gases or materials leads to its identification, the use of a reference beam or measurement is required. Due to changes in amplitude and phase between this reference and the sample measurement, unique spectral features can be located, inferring the materials used in the sample under study. Contrasting with applied reflection spectroscopy for NDE, surveyed in Section 1.2, the reliability of spectroscopic information in this area is limited since the required reference measurement for spectroscopy is not available. With limited spectral information from a sample, some amount of previous knowledge of possible materials present may be required. Because of this, applications often revolve around detecting irregularities and delaminations from immediate changes in the scanning waveform. The time delay of a signal is primarily inspected to detect changes in position, thickness, and refractive index. In addition, some materials are less reactive to THz frequencies, leaving no sharp, detectable spectral features in this range.

1.4 Motivation

The reports discussed throughout this review have outlined common limitations to THz imaging and spectroscopy for practical purposes. Since the development of stable THz sources, the common problem has been favouring the implementation of THz sources for imaging over other frequencies of radiation for NDE. THz frequencies can be more easily absorbed than microwaves, especially in thick materials or in materials having a high moisture content. The high absorption from atmospheric moisture hinders applications for long distance imaging with THz. Regarding the application of THz imaging for corrosion NDE beneath rubber tiles, the high absorption of THz frequencies has limited the practicality of these applications. A similar issue is found in evaluating wooden building products with THz radiation. In the papers reviewed, a repeated limitation of the experiments for reflection imaging and spectroscopy is the lack of a better signal processing technique. In many of the papers investigating reflection imaging of concealed interfaces, the reflected pulses detected provide a large amount of information, that is not always analyzed to its full extent.

In many cases, a change in the amplitude or phase of the signal suggests a change in the material or quality of material at the interface. Most often, water or metal is detected based on a large reflection, or a larger absorption. It is expected that there exists a spectroscopy technique that can gather information from the reflected signals to distinguish between different metals, water or other materials. This is often not regarded in the field of NDE of concealed interfaces for corrosion. In other words, in most systems, there is no need to distinguish between a highly reflective metal and highly absorbent water sample. In a similar manner, there has been plenty of research investigating the detection of damage or corrosion, but less research on identifying areas filled with water or of high moisture content *before* corrosion takes place.

The ability to detect failing systems involving metallic articles or structures due to indications of *pre-corrosion* is a cost-effective and conservative step crucial for industrial applications of THz in NDE, which this thesis aims to explore. In Section 1.2, an application of THz reflection imaging towards the identification of water-filled gaps within submarine tiles is outlined. Based on the expectation of detecting one of two materials, water or air gaps, the detection of water intrusion in a dielectric system protecting a vulnerable metallic system is performed *before* corrosion can take place. This is an appealing conceptual example of a proactive NDE technique that may substantially benefit applicable industrial systems involving insulated metallic structures and water.

This thesis aims to focus on identifying the difference between metallic and water interfaces, along with identifying other dielectric materials, in an insulated, layered system in order to display the practicality of detecting indicators of *pre-corrosion*, as well as emphasizing the importance of these proactive NDE measures to industry. By combining techniques from lab-based THz reflection spectroscopy as well as those from the applications in THz NDE, the goal of this thesis is to explore the ability to conduct reflection imaging at an interface while trying to identify the interface material without the use of a reference measurement.

Chapter 2

THz Time-Domain & Reflection Spectroscopy

For many years, there has existed a slow progression in research involving frequencies constrained by the existence of the THz gap [32]. However, the advancements in optics and electronics technologies towards the 1990s have catalysed the leap of certain technologies leading to the commercialization of THz spectroscopic and imaging systems [33]. The main cause of this leap is the development and implementation of the fs laser source [34]. These extremely short-pulsed laser sources have opened the gate for a novel means of THz pulse generation and coherent detection, generating a surge in publications throughout the 2000s. With access to time-domain information regarding the changing electric field of an electromagnetic pulse, more accurate measures have been discovered for the determination of optical properties of materials using THz radiation. With the use of these spectrometers [35] beginning in the early 2000s, new means of stable THz generation and detection have been adopted. Originally, these methods have relied on photoconducting switches or antennas [36–38] to generate and detect this form of radiation, and have subsequently expanded to include the use of optical rectification and electro-optic sampling [39, 40]. These two methods are not the only forms of generating and detecting this range of wavelengths, but they are quite common in THz-TDS systems. Since the Picometrix® THz-TDS system involved in this thesis revolves around the generation of THz pulses using photoconductive antennas, this is the sole mechanism discussed.

2.1 Generation & Detection of THz Pulses with Photoconductive Antennas

The Picometrix® THz-TDS system employed in this work performs pulsed THz generation and detection by illuminating photoconductive antennas (PCA). For the generation of THz pulses specifically using a PCA, an *ultrafast* fs laser produces a pulse of radiation having a duration of less than 1 ps [41]. Femtosecond lasers typically operate in the near-infrared, usually around 800 nm wavelengths. These ultrashort optical pulses are incident on a PCA, and the resulting THz pulse emitted is a result of the structure of a PCA and the carrier dynamics within a biased semiconductor [42].

The structure of a PCA is comprised of an electronically biased metallic dipole antenna prepared on a semiconductor substrate, as seen in Figure 2.1. The characteristic distances of the antenna such as the dipole length, D, and the gap width, G, directly affect the wavelengths of the radiation emitted. The dipole length is often around 100 μm, and the gap width can be as low as several microns [43]. The absorbed optical pulse supplies sufficient photon energy exceeding the band gap of the semiconductor resulting in excited electrons from the valence band to the conduction band, generating photocarriers within the semiconductor. These photocarriers are accelerated by the electric field of the bias, transmitting a transient electric current density, J. This short-lived, rapidly changing current density

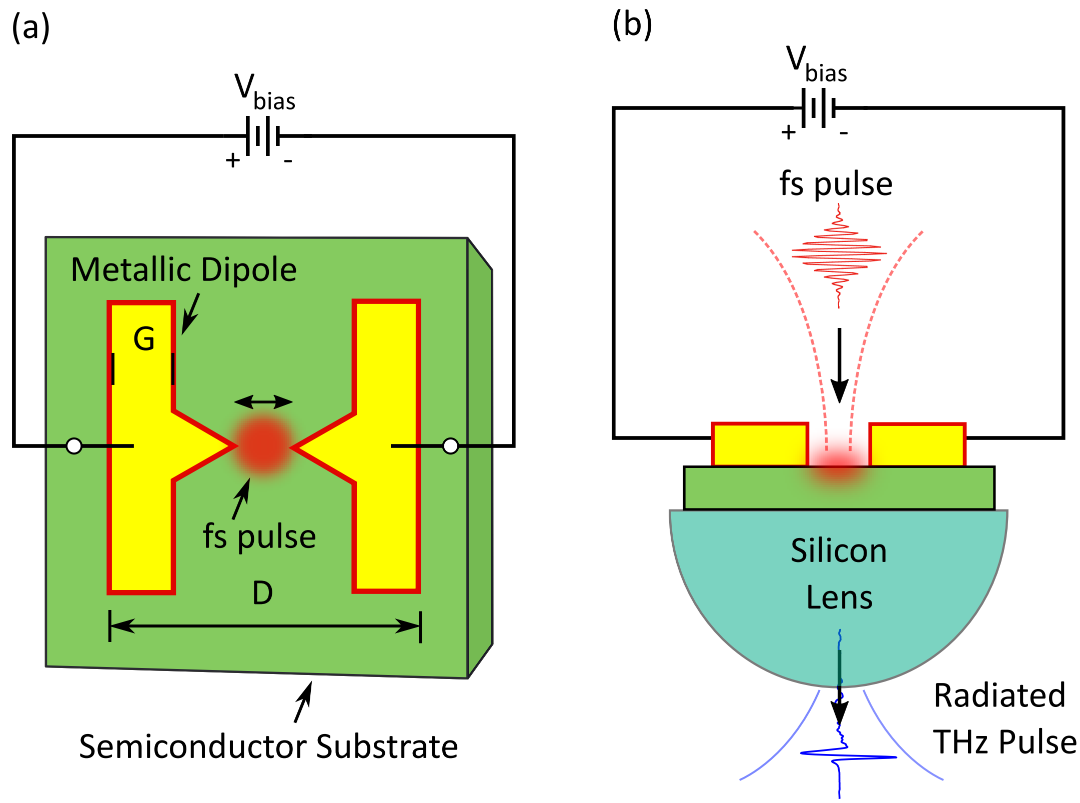

Figure 2.1: (a) A top view of the metallic dipole prepared on the semiconductor substrate with dipole length, D, gap width, G and electronic bias, V_{bias}. The optical femtosecond pulse pumps the center of the antenna. (b) A side view of the PCA emitting a THz pulse focussed by a silicon lens.

drives the dipole antenna which emits a THz pulse, where $E_{THz} \propto \frac{dJ}{dt}$ [42].

The coherent detection of THz pulses with a PCA can be understood comparably to the way it is used for THz generation. The main difference is that the electric field of the THz pulse incident on the detecting PCA works as the bias for the antenna which creates a photocurrent. This current is gated by ultrashort optical pulses on the opposite side of the PCA which samples the electric field of the THz pulse. Incidence of these sampling pulses on the PCA allows for conduction of the transient photocurrent, creating the THz signal, which is a current proportional to the THz electric field, when the optical pulse-width is sufficiently short and the carrier lifetime of the antenna substrate is also short. In order to sample the entire electric field of the THz pulse, multiple optical pulses used for gating the PCA are given different time delays along a delay line relative to the optical pulses used for generation [42], which allows the THz electric field amplitude to be mapped out in time.

The most common semiconductor material for use in PCAs with THz pulses is low temperature grown GaAs (LT-GaAs). The role of this semiconducting substrate is well established in ultrashort pulse photonics due to its adequate carrier mobility and sub-picosecond carrier lifetime. Minimizing the carrier lifetime is of high interest for the creation of quickly changing transient pulses, increasing the bandwidth of emitted THz pulses and associated detection [44]. A frequent interest in emitter/detector systems is the reduction of noise. A primary source of noise within PCAs is Joule heating, a consequence of the conduction of electrical current. Collier et al. studies the application of textured semiconductors in PCAs to reduce charge-carrier lifetimes, minimizing the degree of Joule heating [45]. With the generation of THz pulses and its coherent detection using PCAs, the implementation of THz-TDS is made possible.

2.2 THz Time-Domain Spectroscopy

The emergence of THz-TDS techniques sets the stage for the most common practice of examining optical properties of materials and sampling the interaction of THz frequencies with matter by analyzing spectral information. From the prominence of THz-TDS, many publications in THz science involve the cataloguing of absorption spectra, refractive indices, and other optical properties of dielectrics, gases and metals. As discussed in Section 2.1, the generation and coherent detection of THz pulses using PCAs results in the sampling of the electric field waveform in the time-domain. Measurements of an electric field pulse with respect to time can provide spectral information from the pulse by applying a fast-Fourier transform (FFT) of the time-domain data. This transforms the data into the frequency-domain, providing an individual look at the interaction of specific frequencies with a sample within the bandwidth of the broadband THz pulse [46].

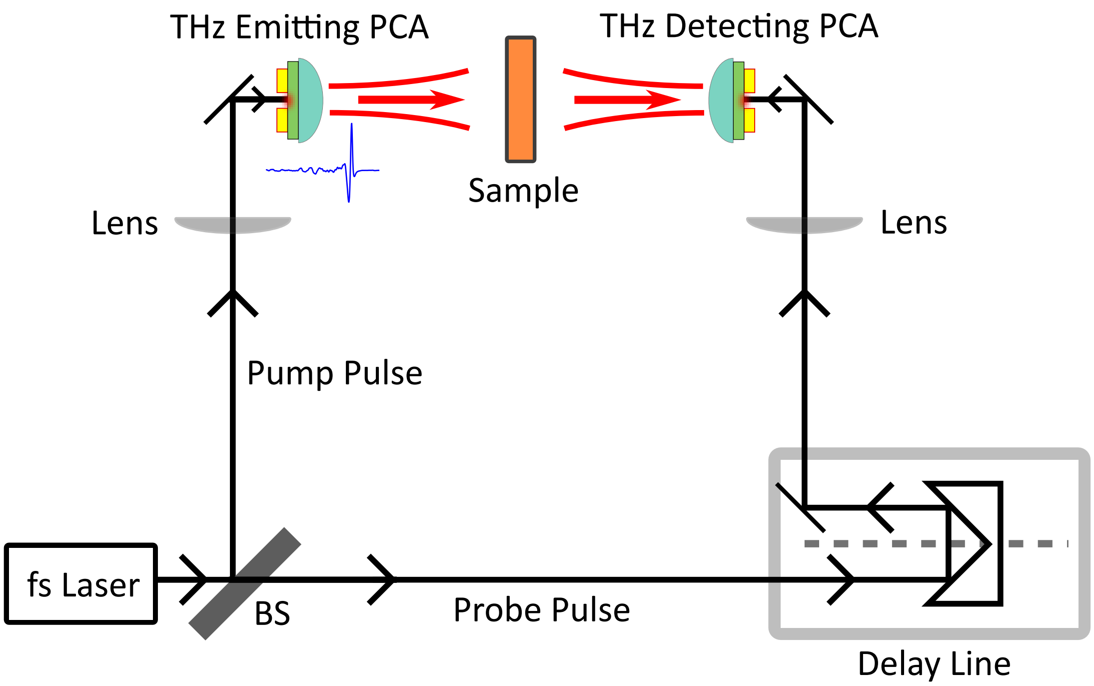

Figure 2.2: A schematic for a typical THz-TDS system using PCAs for the generation and detection of THz pulses. [BS - beam splitter.]

The schematic in Figure 2.2 summarizes a simplified THz-TDS system. Beginning at the *ultrafast* fs laser, a pulse on the order of 100 fs is split by a beam splitter into two identical pulses: the generating pulse directed towards the emitting PCA, and the sampling pulse directed towards an optical delay line before reaching the detecting PCA. The THz pulse emitted by the emitting PCA transmits or reflects from a sample towards the detecting PCA. As the delay line is adjusted, different points along the THz waveform are measured and plotted in the time-domain [47]. For each different delay line position, the time value of the electric field data point is altered accordingly. Optics such as lenses and mirrors for redirecting or focussing optical pulses are excluded from the diagram to clearly illustrate the operation of the system. The THz-TDS is capable of performing in the transmission and reflection modes. This spectroscopic system is often used in THz imaging as well. By raster scanning a sample within the apparatus described above, these THz pulse measurements can be gathered in a spatial configuration. Signals are often converted to the frequency-domain to obtain spectroscopic information from the THz pulse for each pixel of the gathered image. Not only can spatial spectroscopic information be gathered, but given the time-domain measurements, time-of-flight analysis can be performed to determine depth characteristics of the given imaging sample [48].

2.3 Modelling a THz Pulse

Electromagnetic (EM) radiation, or EM waves, are represented in terms of the corresponding electric and magnetic fields, $\vec{E}$ and $\vec{B}$, respectively, which are in phase, simultaneously varying in time, and perpendicular to each other in space. The electric field of a plane wave can be represented in time in terms of the amplitude E_o, the wave number k, and angular frequency ω.

$$\vec{E} = \vec{E}_o e^{i(\vec{k}\vec{r}-\omega t)} = \vec{E}_o e^{i\phi} \tag{2.1}$$

The direction of the cross product between $\vec{E}$ and $\vec{B}$ indicates the direction of the wave propagation, parallel to $\vec{k}$. For an EM wave given by equation (2.1), it is essential to define the orientation of the wave with respect to the plane of incidence (POI) along which reflection and transmission of the EM wave occurs. The POI is defined as the plane containing the wavevector $\vec{k}$ and the surface unit normal vector $\hat{n}$ of the boundary plane where reflection and transmission occur. At the

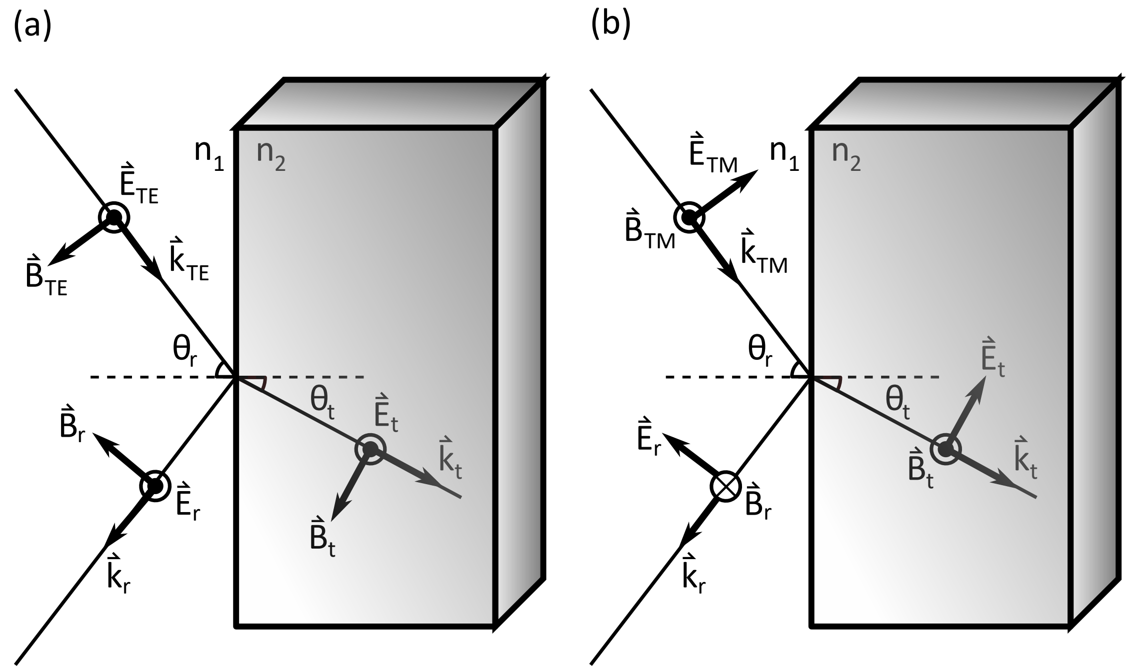

Figure 2.3: The propagation of an electromagnetic wave at an interface between two media, n_1 and n_2. For the (a) TE and (b) TM polarizations, the reflected and transmitted electric fields $\vec{E}$ and magnetic fields $\vec{B}$ are shown as vectors, along with the corresponding wavevectors $\vec{k}$. The POI is parallel with the page, and the boundary plane is perpendicular to the page.

intersection of the POI and the boundary plane, the boundary conditions (inherent from Maxwell's equations) are applied to the electric and magnetic fields of the incident wave to determine the behaviour of the resulting electromagnetic waves, following incidence with the boundary. Since these boundary conditions require the continuity of the portion of the electric field that is parallel to the boundary plane, as well as the portion of the magnetic field that is perpendicular to the boundary plane, two unique (and convenient) polarization modes of an EM wave are introduced [49]. If $\vec{E}$ is perpendicular to the POI, then this is referred to as *transverse electric* (TE) polarization. Conversely, in the case that $\vec{B}$ is perpendicular to the POI, the EM wave has *transverse magnetic* (TM) polarization.

Upon reflection at an interface between two different media, the Fresnel equations determine the fraction of the electromagnetic field amplitude reflected and transmitted. Since the reflectance and transmittance of an electromagnetic wave at an interface are sensitive to polarization, the reflection coefficients are given for both TE and TM polarizations. For an incident EM wave having an electric field E_i, the reflected electric field $E_r \equiv rE_i$ is determined by the amplitude reflection coefficient r given below for the TE polarization

$$r_{TE} = \frac{\cos\theta - \sqrt{n^2 - \sin^2\theta}}{\cos\theta + \sqrt{n^2 - \sin^2\theta}}, \tag{2.2}$$

as well as the TM polarization

$$r_{TM} = \frac{-n^2\cos\theta + \sqrt{n^2 - \sin^2\theta}}{n^2\cos\theta + \sqrt{n^2 - \sin^2\theta}}, \tag{2.3}$$

where θ is the angle of incidence on the boundary, and $n \equiv \frac{n_2}{n_1}$ is defined by the fraction of the refractive indices n_1 for medium 1 (incident) and n_2 for medium 2 (transmitted), which form the interface. Similarly, for the transmitted portion of the EM wave, transmission coefficients are used to determine the transmitted electric field amplitude. The equations for the amplitude transmission coefficients can be simplified for normal incidence (wave propagation orthogonal to the surface plane). Only the simplified transmission coefficient equation with $\theta = 0$ is shown as this thesis deals primarily with the reflected waves.

$$t_{12} = \frac{2\tilde{n}_1}{\tilde{n}_1 + \tilde{n}_2} \tag{2.4}$$

In equation (2.4), $\tilde{n}_1$ and $\tilde{n}_2$ are the complex refractive indices for medium 1 and 2, which are generally defined in terms of the real refractive index $n(\omega)$ and the extinction coefficient $\kappa(\omega)$ as in equation (2.5).

$$\tilde{n}(\omega) = n(\omega) + i\kappa(\omega) \tag{2.5}$$

The extinction coefficient is dominant in metals and conducting materials, and it is directly related to the absorption coefficient $\alpha(\omega)$ of the medium as follows:

$$\kappa(\omega) = \frac{\alpha(\omega)c}{2\omega} \tag{2.6}$$

where c is the speed of light in a vacuum ($c = 3 \times 10^8 m/s$).

These equations are often used in various methods of reflection spectroscopy in order to determine optical and material properties of a sample medium present at the reflecting interface because THz spectroscopy is sensitive to the electric field directly, and consequently probes the complex index of refraction directly (both real and imaginary parts). Conventionally, a common focus in spectroscopy is the use of a reference and sample measurement. By controlling all components of an optical system for a reference measurement, followed by the introduction of a sample into the optical system for the sample measurement, a ratio of these two measurements can reveal optical information for the sample material by mathematically inverting the Fresnel equations in combination with the measured data. This technique allows for the determination of optical and material properties of a sample, as well as the identification of materials. This general method is explicitly outlined in the following sections, first by a simplified transmission spectroscopy model, and next, in the context of a unique form of reflection spectroscopy involving a dove prism.

2.4 THz Transmission Spectroscopy

The use of THz-TDS in the transmission mode excels in the extraction of dielectric properties of many insulating materials, in which THz frequencies can propagate with low losses. As the noise floor is approached at higher frequencies within the bandwidth of a spectrometer, transmission spectroscopy becomes less reliable [31].

This causes heavily absorbing materials to be difficult to determine via transmission spectroscopy. In this field, outlining the assumptions made for a given transmission spectroscopy technique is important. Typically, it is assumed that material properties are homogeneous with respect to position and direction, and that interfaces between media are flat and parallel to each other, also neglecting scattering [50]. Unless otherwise specified, the atmosphere is assumed to be dry and uniform in temperature, and its absorption is ignored. One key assumption that allows the use of the simplified transmission coefficient given by equation (2.4) is taking the angle of incidence θ to be zero, or assuming *normal incidence*. This allows the change in path of propagation introduced by refraction to be ignored. The last assumption to be made for this transmission spectroscopy technique is introduced as the *thick sample* approximation.

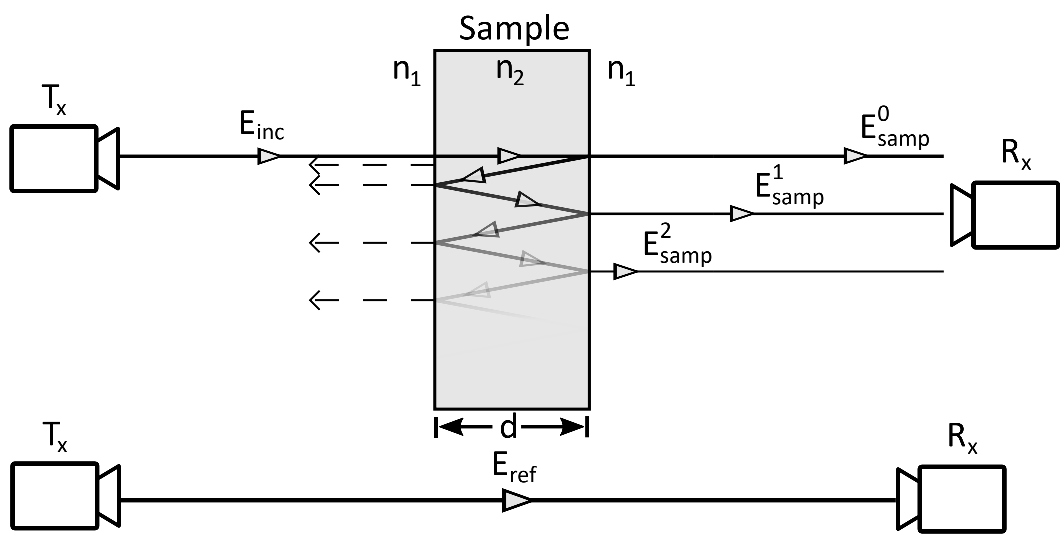

Figure 2.4: An illustration of Fabry-Pérot reflections from an incident electric field E_{inc} transmitting through a sample having a refractive index of n_2 surrounded by air, $n_1 = 1$. These F-P reflections cause multiple THz pulses to be detected at different time delays. The electric field at the bottom of the figure represents a reference measurement E_{ref}. [T_x - transmitter, R_x - receiver.]

As an electric field approaches a sample with optically flat and parallel edges, a portion of the electric field is reflected and transmitted into the sample. The transmitted portion undergoes multiple reflections within the sample, referred to as Fabry-Pérot (F-P) reflections. At each consecutive reflection, a weaker electric field is transmitted outside of the sample as sketched in Figure 2.4. In the context of detecting THz pulses transmitting through a sample at normal incidence, multiple pulses are detected at different time delays. For the case of a thin sample, these pulses are separated by a very small time delay, calling for complex analytical methods to interpret the measured electric field. In the case of a thick sample, these reflections have relative time delays such that the first transmitted pulse can be captured and isolated within the time window of the THz-TDS system, and the more simple analytical method can be used. Assuming thick samples are used for this method in this thesis, modelling of only the 0^{th} transmitted pulse in Figure 2.4 is sufficient for the determination of $\tilde{n}(\omega)$ and $\alpha(\omega)$, as in Duvillaret et al. [51].

In order to determine the index of refraction $n(\omega)$ and the absorption coefficient $\alpha(\omega)$ of a sample, a reference THz pulse $E_{ref}(t)$ as well as a sample THz pulse $E_{samp}(t)$ need to be collected to measure the effect of the sample on the propagation of the THz pulse. The fast-Fourier transform of the pulses are then taken, giving $E_{ref}(\omega)$ and $E_{samp}(\omega)$, and since dielectric properties are dependent on frequency, the spectroscopic information from these pulses are analyzed. Since the propagation of an electric field through the system is complicated, the construction of a transfer function experimentally $H_{exp}(\omega)$ and theoretically $H_{th}(\omega)$ is a vital aspect to creating a solvable problem:

$$H_{exp,th}(\omega) = \frac{E_{samp}^{exp,th}(\omega)}{E_{ref}^{exp,th}(\omega)}. \tag{2.7}$$

The reference and sample measurements allow $H_{exp}(\omega)$ to be calculated, however $H_{th}(\omega)$ remains to be evaluated.

In order to build the physical representation of the reference and sample electric fields, E^{th}_{ref} and E^{th}_{samp}, propagation effects must be included. When an initial electric field propagates some distance in any medium, the resulting electric field is determined by a propagation coefficient [52]. For an electric field E_o propagating a distance z through medium 1, the propagation coefficient $P(\tilde{n}_1, z)$ is as follows:

$$P(\tilde{n}_1, z) = \exp\left(\frac{-i\omega\tilde{n}_1 z}{c}\right). \tag{2.8}$$

Applying this coefficient to the initial electric field E_o gives the resulting electric field $E(z)$ in the following equation:

$$E(z) = E_o P(\tilde{n}_1, z). \tag{2.9}$$

Using propagation coefficients and transmission coefficients and referring to Figure 2.4, E^{th}_{ref} and E^{th}_{samp} can be built to determine $H_{th}(\omega)$. Since the reference pulse E^{th}_{ref} propagates solely through air ($n_1 = 1$) over an arbitrary distance L between the source and detector, it can be given simply by $E^{th}_{ref} = E_o P(\tilde{n}_1, L)$. For the sample pulse E^{th}_{samp}, the pulse propagates through a width d in the sample medium 2, as well as propagating in air for a distance $L - d$. Transmission from medium 1 to 2 and back to 1 also introduces coefficients, t_{12} and t_{21}, given by equation (2.4). The sample pulse can then be given as $E^{th}_{samp} = E_o P(\tilde{n}_1, L-d) t_{12} P(\tilde{n}_2, d) t_{21}$, thus the theoretical transfer function is constructed as follows:

$$H_{th}(\omega) = \frac{E^{th}_{samp}}{E^{th}_{ref}} = P(\tilde{n}_1, -d) t_{12} P(\tilde{n}_2, d) t_{21} \tag{2.10}$$

since $P(\tilde{n}_1, L-d)/P(\tilde{n}_1, L) = P(\tilde{n}_1, -d)$.

After equating equations (2.7) and (2.10) to set $H_{exp}(\omega) = H_{th}(\omega)$, then using equation (2.8) to insert the propagation coefficients, the following equation arises:

$$H_{exp}(\omega) = t_{12} t_{21} \exp\left[\frac{-i\omega d}{c}(\tilde{n}_2 - 1)\right]. \tag{2.11}$$

It should be noted that $\tilde{n}_1 = 1$ for air, t_{12} and t_{21} do not have complex components throughout this configuration, and $\tilde{n}_2 = n_2 + i\kappa_2$ from equation (2.5). By using a form of Euler's equation to express equation (2.11) as $H_{exp}(\omega) = A(\omega)e^{i\phi(\omega)}$, the absolute value $|H_{exp}|$ and the argument $arg(H_{exp})$ of equation (2.11) can be used to extract the index of refraction $n_2(\omega)$ and absorption coefficient $\alpha_2(\omega)$ of the sample.

The representation of the index of refraction is a consequence of analyzing the phase $\phi(\omega)$ of the transfer function, letting $\phi(\omega) = arg[H_{exp}(\omega)]$. From equation (2.11) it is evident that this phase $\phi(\omega)$ becomes

$$\phi(\omega) = \frac{\omega d}{c}[n_2(\omega) - 1] \tag{2.12}$$

which can then be rearranged to give the following relationship for the index of refraction $n_2(\omega)$:

$$n_2(\omega) = \frac{c}{\omega d}\phi(\omega) + 1. \tag{2.13}$$

Similarly, the absorption coefficient can be determined by inspecting the amplitude $A(\omega)$ of the transfer function, letting $A(\omega) = |H_{exp}(\omega)|$. Again, from equation (2.11), and substituting Fresnel's transmission coefficients and complex index of refraction with equation (2.4) and (2.5), respectively, the following equation emerges:

$$|H_{exp}(\omega)| = \frac{4n_2(\omega)}{[n_2(\omega) + 1]^2} \exp\left[\frac{\kappa_2(\omega)\omega d}{c}\right]. \tag{2.14}$$

Note that in the determination of Fresnel's transmission coefficients, the approximation $n \gg \kappa$ is used. For optically transparent (low absorption) materials at THz frequencies, this approximation holds. Finally, by using the relationship between the extinction coefficient $\kappa_2(\omega)$ and absorption coefficient $\alpha_2(\omega)$ in equation (2.6), the relationship yielding the absorption coefficient becomes

$$\alpha(\omega) = -\frac{2}{d} \ln\left\{A(\omega)\frac{[n_2(\omega)+1]^2}{4n_2(\omega)}\right\}. \tag{2.15}$$

To conclude, the determination of the index of refraction $n_2(\omega)$ depends strictly on the phase $\phi(\omega)$ of the transfer function constructed by the reference and sample measurements in the frequency domain, as well as the angular frequency ω and thickness of the sample d. Adding a small amount of complexity, the absorption coefficient essentially depends on the angular frequency ω, thickness d, amplitude $A(\omega)$ *and* phase $\phi(\omega)$ of the same transfer function. As a reminder, the thick sample approximation assumes roughly that $2n_2(\omega)d/c > t_{window}$, where t_{window} is the length of the spectrometer time window, thus thick *or* high index materials are sufficient.

2.5 THz Dove Prism Reflection Spectroscopy

The use of a dove prism in THz-TDS is a common technique when exploring reactive optical properties of materials. A dove prism is a component of an optical system that takes the geometrical form of a trapezoidal prism, in which the two angled, rectangular faces can be described as the input and output for incident plane EM waves. Throughout the course of this thesis, THz pulses in the time-domain spectrometer are modelled similarly to a plane wave. Each pulse is a superposition of plane waves at different frequencies, thus for analysis, a fast-Fourier transform is often applied to measured pulses in order to study the electric field at each frequency. Provided by its shape and orientation displayed in Figure 2.5, there are many convenient features of dove prisms for determining reflecting properties of a sample. After a horizontal EM wave propagates through the dove prism, it is returned to its initial propagation direction, allowing for quick alignment. The flat top face also simplifies the testing of sample materials, especially liquids.

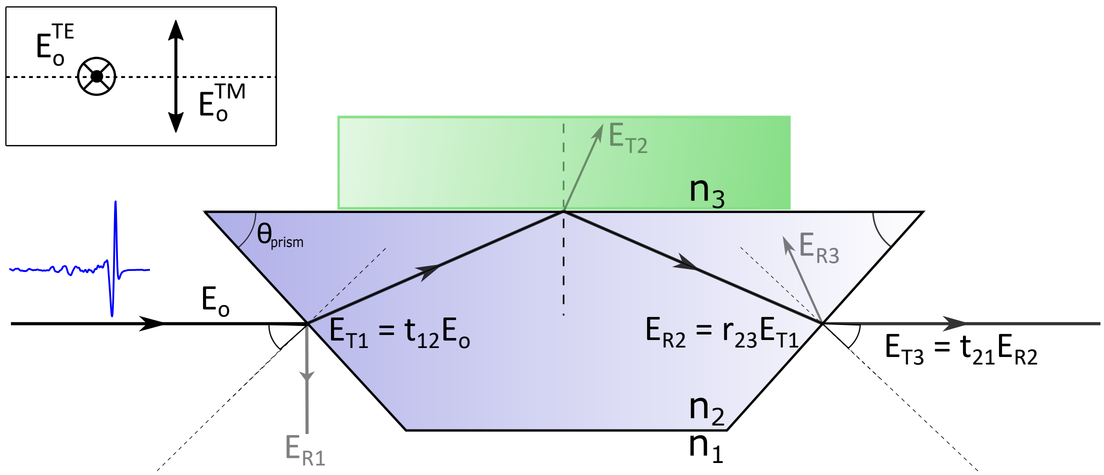

Figure 2.5: The path of propagation of a THz pulse within a dove prism (n_2) used for reflection spectroscopy of a sample (n_3). Reflected and transmitted electric fields are expressed with respect to the appropriate Fresnel coefficient. The detected pulse is determined in terms of the initial electric field E_o. The key purpose of this diagram is to draw attention to the cause of changes in the detected pulse when only the sample (n_3) is changed.

Figure 2.5 illustrates the optical path of propagation of a THz pulse as a plane EM wave within the dove prism. In a typical THz-TDS apparatus, the measured current or voltage directly relates to the electric field of the THz pulse, so the focus is on the determination of the electric field of a given THz pulse throughout the dove prism. Considering a THz pulse travelling horizontally with an electric field E_o in medium 1 incident on the first angled face of the dove prism, a small amount is reflected downwards giving E_{R1} and the remainder is transmitted from medium 1 into medium 2 giving $E_{T1} = t_{12}E_o$, refracting towards the top face of the dove prism. The next boundary involves the interface of the dove prism and the sample, medium 2 and medium 3. Upon reflection at this interface, the THz pulse

$E_{R2} = r_{23}E_{T1} = r_{23}t_{12}E_o$ travels along a path symmetric to its previous propagation. Following the refraction back into medium 1 from medium 2, the electric field E_f (re-labelling E_{T3} from Figure 2.5 for convenience) of the output (horizontally travelling) THz pulse is detected.

$$E_f = E_{T3} = t_{21}E_{R2} = t_{21}r_{23}t_{12}E_o \tag{2.16}$$

In order to model reflections within a dove prism, or to use reflections to determine optical properties of a sample material, the use of a type of transfer function is vital. By taking a reference measurement, as well as a measurement with the sample on the top face of the dove prism, the ratio of these measurements results in the cancellation of unnecessary components from equation (2.16). Considering these two measurements, the only part of the optical system that is not kept controlled is medium 3, thus the theoretical transfer function H_{th} can be constructed as shown below

$$H_{th} = \frac{E_{sam}}{E_{ref}} = \frac{t_{21}r_{sam_{23}}t_{12}E_o}{t_{21}r_{ref_{23}}t_{12}E_o}, \tag{2.17}$$

and the simplified relationship for dove prism reflection spectroscopy is illustrated as follows:

$$\frac{E_{sam}(\omega)}{E_{ref}(\omega)} = \frac{r_{sam}(\omega)}{r_{ref}(\omega)}. \tag{2.18}$$

It is noted that the reflection coefficients for the interface between medium 2 and medium 3 have been renamed r_{ref} and r_{sam} for the reference and sample measurements, respectively.

In the simplified equation (2.18), the ratio of the measured reference and sample electric fields is equivalent to the ratio of the corresponding reflection coefficients. Using this approach, the equation is rearranged to solve for $E_{sam}(\omega)$ in order to predict the reflected electric fields from a sample material. Equation (2.18) becomes

$$E_{sam}(\omega) = \frac{r_{sam}(\omega)}{r_{ref}(\omega)} E_{ref}(\omega) \tag{2.19}$$

where $r_{sam}(\omega)$ and $r_{ref}(\omega)$ are calculated using equations (2.2) or (2.3). This requires a reference measurement as well as the refractive index of the dove prism material $n_2(\omega)$ and that of both the reference and sample material $n_3(\omega)$ for the appropriate angular frequency ω.

This approach can also be used to solve for $r_{sam}(\omega)$ in order to determine the reflectance of a sample material of unknown optical properties. Equations (2.2) and (2.3) can then be used to calculate the refractive index of the unknown sample. It is important to note that in spectroscopy and NDE applications, the transfer function detailed in equation (2.17) is often used to detect subtle differences in two measured waveforms, one being the reference. From equation (2.1), relative changes in amplitude and phase can be easily calculated and illustrated using a ratio of the corresponding electric fields. This is often the main focus in many practical cases since a single measurement of an electric field from a complex system is difficult to analyze. For the identification of a sample material, a reference measurement is required, and in this way, the index of refraction and absorption coefficient of the sample can be calculated.

Chapter 3

Experimental Methods

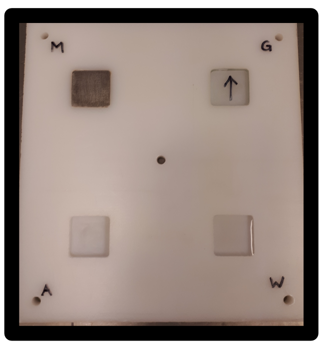

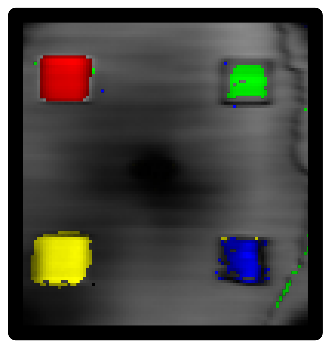

After establishing a theoretical model for the reflection of an electromagnetic wave at a concealed interface, a dove prism is used to compare measured reflections to predicted reflections for varying interfaces. The geometry of a dove prism allows for convenient and quick testing of different samples in search of significant, qualitative differences in the reflections at a selected interface. Those interfaces that result in reflections having drastic inversions or changes in shape relative to a reference reflection can then be implemented in a similar configuration to be imaged (e.g. a layered system concealing the corresponding interfaces). For a given sample in contact with the face of an ultra-high molecular weight polyethylene (UHMW-PE, or UHMW) dove prism, the measured THz pulse at the output of the dove prism represents the reflection of the incident pulse from a UHMW-sample interface. Not only can this configuration distinguish between contrasting reflecting interfaces, but it can also reveal which polarization configuration will be most sensitive for this purpose. The dove prism simplifies reflection measurements from a UHMW-sample interface as opposed to repetitively swapping samples concealed by layers of UHMW which introduces errors in time-domain measurements from moving the interface in between measurements. The use of a dove prism in the first part of the experimental methods is of great importance in order to determine which interfaces are to be involved in the imaging sample in the later section of the experiment and in what polarization the imaging beam is to be aligned. After determining four materials that each produce a differing reflected waveform in the dove prism, these materials are concealed within a layered UHMW system to imitate a system in an applied, real-world setting. Using THz frequencies, the layered sample is imaged by means of a raster scan in order to spatially locate and identify the concealed materials.

3.1 Apparatus

3.1.1 Pulsed Terahertz Controller

The THz-TDS source and detection system used in this thesis is a modified T-Ray® 4000 pulsed THz controller patented by Picometrix®. The enclosed system produces and detects THz pulses on the order of picosecond durations by the use of a 1064 nm fs laser with fiber-coupled emitter and detector heads as shown in Figure 3.1. The heads allow for the propagation of THz pulses through an experimental system before detection in order to examine properties of the system at THz frequencies. Broadband THz pulse measurements from 0.02 THz to 2 THz can be measured within an 80 ps time window with a data collection rate of 1000 Hz. The T-REX computer software displays and analyzes detection measurements for real-time monitoring or recording of THz waveforms for experimental analysis. A

Figure 3.1: A photograph of (a) the pulsed THz controller and (b) an emitter and detector head. The optical cables couple each head to the corresponding transmitting/receiving plug. The dual-channel setup allows two emitter/detector pairs to be operating simultaneously.

newer model of this system is the T-Ray® 5000 available through Picometrix®, a subsidiary of Advanced Photonix Inc [53]. The system is used in a transmission (Section 3.2) and two separate reflection geometries (Section 3.4) throughout this thesis.

3.1.2 Dove Prism

The dove prism is designed in order to conveniently create and examine interfaces that are to be concealed in an imaged sample in a later section of the experiment. The dove prism is constructed from a solid block of UHMW material because of its extremely low absorbing properties, which is investigated in Section 3.2 via THz transmission spectroscopy. The block of UHMW has been cut with a band saw to the shape of a 45° trapezoidal prism, and the top face has been sanded to provide a smooth surface. The surface roughness is estimated to be approximately 30 µm, or in terms of wavelength, $\lambda/10$ (at $\lambda = 0.3$ mm wavelength or 1 THz). The specific dimensions of the dove prism are outlined in Figure 3.2. The height and width of 6 cm provide a sufficient area on the angled face of the prism to contain the incident beam of the THz source. The index of refraction of UHMW is 1.52 for frequencies in the range of 0.1 THz to 0.6 THz. Given this value, the selection of an angle of

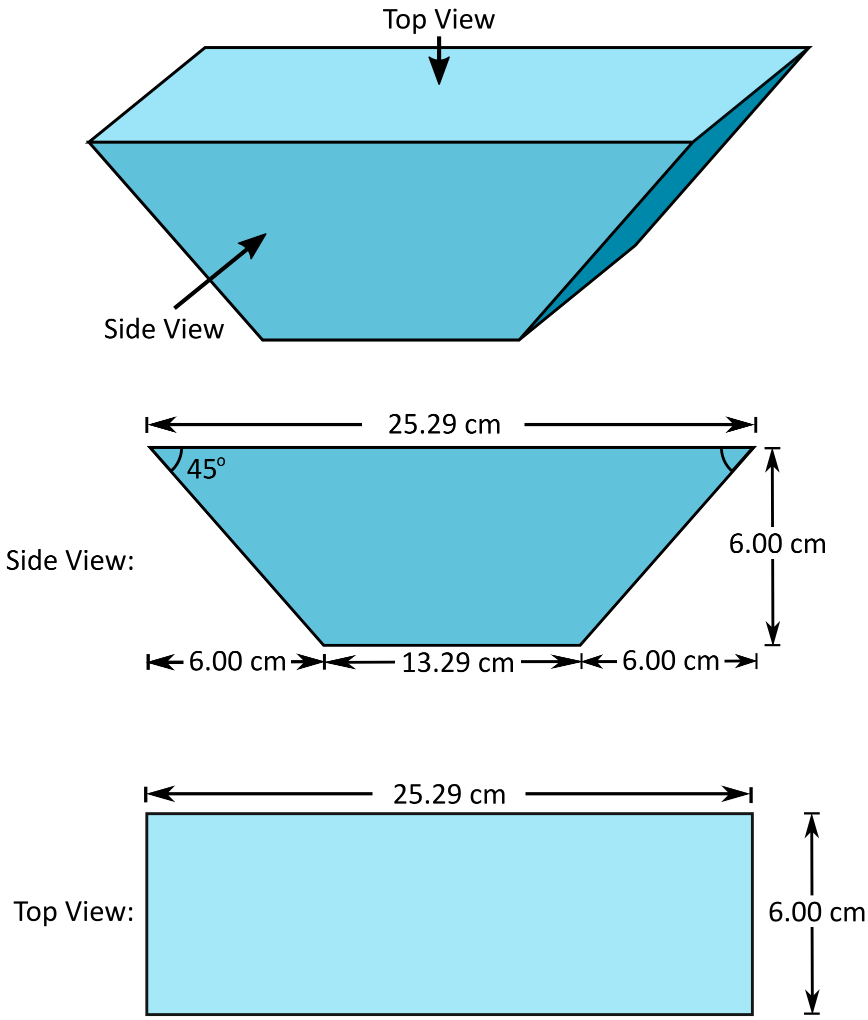

Figure 3.2: The blueprint of the UHMW dove prism used to inspect reflections at chosen UHMW-sample interfaces. Important dimensions and the angle of the prism are outlined and selected such that the input/output THz pulses remain horizontal, considering an index of refraction of 1.52.

incidence of 45° leads to an angle of reflection at the top face of the prism of 73° for these frequencies. The dove prism is mounted onto a secured mechanical jack in the experiment for convenience in alignment.

3.1.3 Imaging Sample

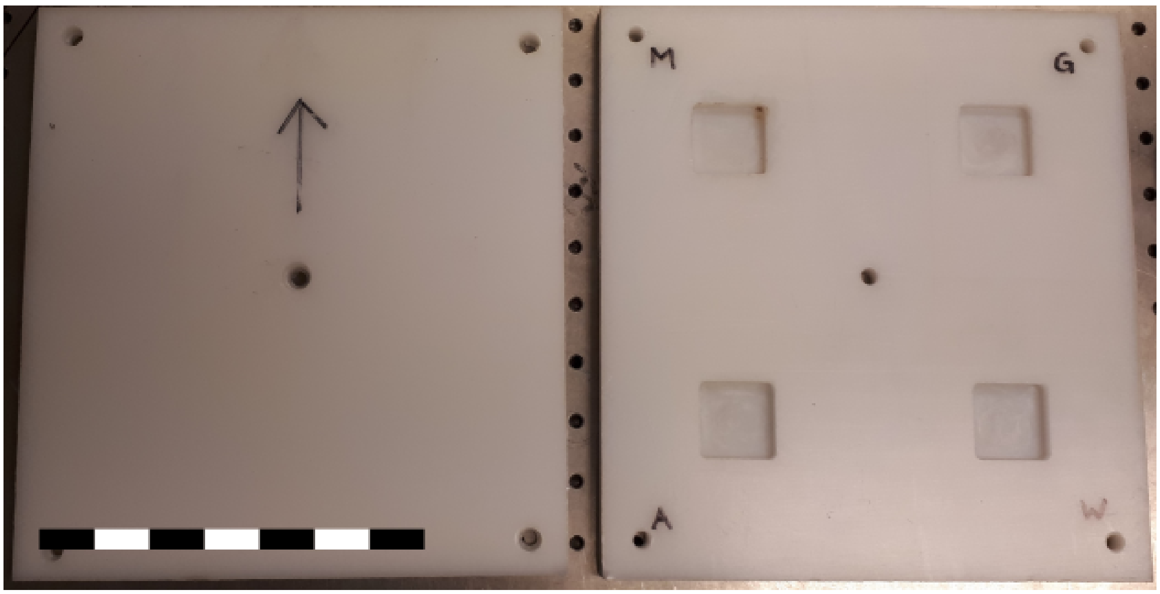

Figure 3.3: A photograph of the dismantled imaging sample at its actual size. The top and bottom sections are shown respectively on the left and right. Each division of the scale bar represents 2.54 cm (1 inch).

The imaging sample is constructed from a slab of UHMW that is 1.27 cm thick. Using a band saw, two identical rectangular pieces, 24.1 cm by 22.9 cm, have been cut from the slab. After dividing one of the pieces into four quadrants, small square sections, 3.2 cm by 3.2 cm, have been milled out at the center of each of the four quadrants at a depth of 0.64 cm as seen in Figure 3.3. The computer numerical control machine at the UNBC Wood Innovation Research Labs is used to create the uniform, square pockets. Next, the two pieces of UHMW are stacked with the edges aligned and clamped together such that the milled-out sections were concealed. Holes are drilled at each corner and in the center of the sample, so the top and bottom pieces in Figure 3.3 can be bolted together. This allows for quick and convenient manipulation of the materials being concealed within the pockets of the sample for imaging purposes later in this thesis. A larger drill bit is used to countersink the bolt heads on the top piece of the imaging sample to provide a smooth top surface.

UHMW-PE is an exceptionally high molecular weight thermoplastic that is extremely abrasion, impact and chemically resistant, the highest among plastics [54]. The surface has very low adhesion, friction and water absorption properties. The material is also very ductile, and it absorbs energy and sound well, although when heated, it maintains a high resistance to deformation, even past its melting point [55]. Many attributes of UHMW hold up even at cryogenic temperatures.

The impressive qualities of UHMW lead it to be a favoured material for many insulating applications, even replacing steel in some applications. Due to its self-lubrication and impact resistant properties, it has been originally used in the handling of bulk materials like grain, cement and gravel, as well as in the mining industry. UHMW can be used in dumping trucks, silos, large bins, conveyor systems, chutes, dry bearings, and so forth [54]. UHMW combined with other substances, such as oil, can be crafted into a fibrous form, which is found in bulletproof vests and protective gloves. Since UHMW is well-established in protective applications involving large amounts of harsh, gritty materials or chemicals, its involvement in the field of NDE is not surprising. Due to its advantageous characteristics, UHMW mostly exists on the outermost layer of many industrial systems in order to prevent wear or damage to the underlying structure of the system. The use of various metals within the underlying structure of these types of systems is also common, posing many risks such as the infiltration of elements from the outside environment, such as water. In Section 3.2, the determination of the dielectric properties of UHMW at THz frequencies is outlined. One key result is the minimal absorption of UHMW at these frequencies. This prompts the investigation of UHMW, in this thesis, for use as the outer material of a layered system imitating a realistic, industrial system, in which various concealed interfaces are imaged in space and identified. The practical importance of the identification of different materials, especially metals and water, concealed by UHMW is also evident from the applications surveyed.

3.2 Transmission Spectroscopy

The analytical method used for transmission spectroscopy of insulating materials such as UHMW and glass is outlined in Section 2.4. Results of transmission spectroscopy include plots of the index of refraction as a function of frequency for the dielectric materials used through the course of this thesis, as well as the inspection of the absorbing properties of UHMW, which motivates the selection of UHMW as the dove prism constructing material. The measurement of the refractive index of glass allows modelling of glass reflections in the reflective mode, described in the later Section 3.3. By taking a set of reference and sample measurements of THz pulses for both materials, illustrated in Figure 2.4, spectroscopic functions for index of refraction and the absorption coefficient are calculated. For an explanation of the setup, the schematic involved in the sketch from Figure 2.4 can be followed.

Setting up the apparatus for the transmission mode is straight-forward, since it involves mounting the transmitting and receiving THz pulse heads with only a sample and aperture in between. After aligning the emitter and detector, the sample and aperture are mounted nearest to the detector, in the respective order. The sample is mounted in the THz pulse path, and a carpenter square is used to align the sample normal to the propagation of the THz pulse.

For the determination of dielectric properties for UHMW, a reference electric field measurement of the THz pulse is taken at a time delay of 1610 ps, captured within an 80 ps time window by the T-REX software in real-time. Three consecutive measurements immediately follow as part of the same reference measurement, each with a time delay translated 80 ps further. The full measurement consists of four 80 ps wide electric field plots, each at 1610 ps, 1690 ps, 1770 ps and 1850 ps, respectively. This allows for a higher resolution in the frequency domain, increasing the degree of accuracy for measuring the dielectric properties. The averaging setting in the T-REX software also automatically averages 1000 THz waveforms for each sampled waveform before recording, in real-time. The reference measurement corresponds to an empty region between the emitter and detector. This technique of data collection is repeated for every measurement in this section. For the sample measurements, the electric field of the transmitted THz pulse through the sample at normal incidence is captured in the same time window as the reference measurement. The sample measurements are taken immediately following the reference measurements to avoid errors from fluctuating temperatures within the optical fibers of the pulsed THz controller that may cause detected values to slightly drift in the time-domain. A 12.7 mm thick sample of UHMW is placed between the emitter and detector during the sample measurements. Following the first two measurements, a total of two measured electric fields are obtained for the reference and the sample, across a time range of 360 ps.

This is repeated five times for averaging purposes. The entire process is repeated for a 6 mm thick glass sample. With the set of measured THz pulse electric fields, the time-domain waveforms need to be analyzed in order to determine the dielectric properties of UHMW (and glass). In Section 3.3, a dove prism can then be constructed according to the optical properties at THz frequencies of UHMW in order to analyze spectral features of materials in the reflection mode, with confidence, which then establishes the foundation of the main focus of this thesis, a deeper look into reflection imaging.

3.2.1 Experimental Results

The analytical method introduced in Chapter 2.4 is implemented in a MATLAB® script in order to calculate values to construct the index of refraction $n(\omega)$ and absorption coefficient $\alpha(\omega)$ at various frequencies in the low-THz range for UHMW and glass. By taking the fast-Fourier transform of the time-domain electric field data $E(t)$, the reference and sample electric field waveforms $\tilde{E}(\omega)$ are calculated along the frequency domain. The transfer function $H_{exp}(\omega)$ from equation (2.7) is constructed by taking the ratio of the transformed electric fields for the sample and reference measurements. Finally by taking the argument and absolute value of the complex data points that generate the transfer function, $\phi(\omega)$ and $A(\omega)$ are obtained and used in equations (2.13) and (2.15) to determine the index of refraction $n(\omega)$ and absorption coefficient $\alpha(\omega)$ with respect to frequency.

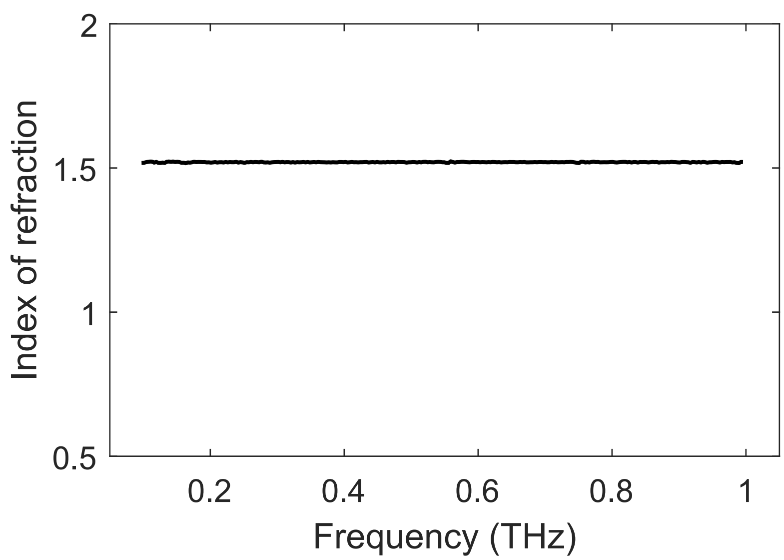

Figure 3.4: The calculated index of refraction $n(\omega)$ of UHMW from 0.1 THz to 1 THz using transmission TDS. The index of refraction is constant at approximately 1.52 from 0.1 THz to 1 THz.

Figure 3.4 displays the index of refraction of UHMW which is essentially constant, around 1.52 over frequencies between 0.1 THz and 1 THz. The absorption coefficient is excluded from Figure 3.4 since it falls to the noise floor over the same frequency range, leading to the conclusion that THz radiation is minimally absorbed by UHMW. Motivated by the interest in designing a dove prism for reflection spectroscopy in Section 3.3, a material which has minimal absorption and a constant index of refraction for frequencies within the bandwidth of the THz-TDS system is ideal for use in the construction of THz optics. To emphasize the importance of low absorption in UHMW, the path of propagation in a dove prism designed for THz frequencies is longer than in most optical instruments, such as lenses and other beam shaping devices, leading to a larger amount of absorption which diminishes the accuracy of spectroscopic information within the THz pulse. The use of UHMW as the primary material of a dove prism for reflection spectroscopy is predicted to be sufficient based on the consistent refractive properties at THz frequencies, as well as its minimal absorbance.

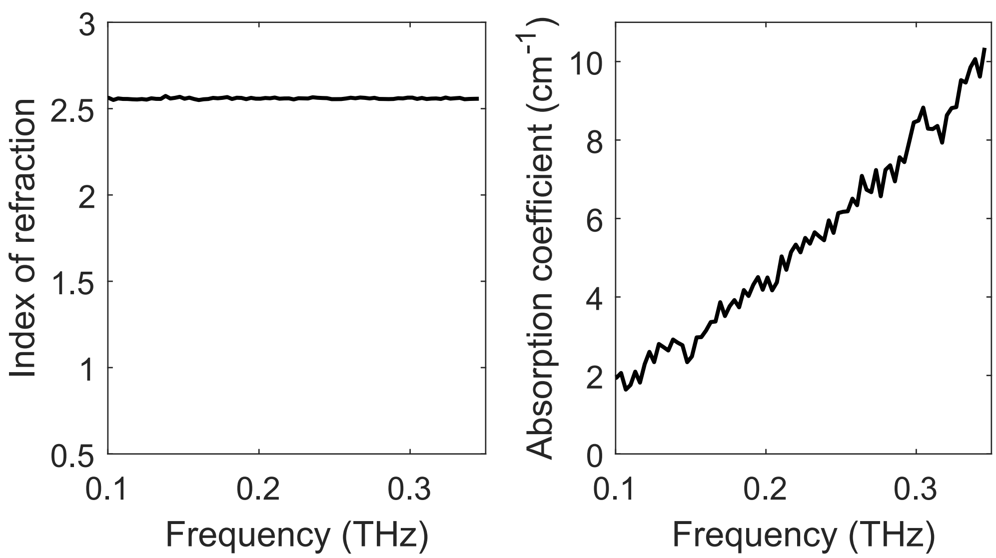

Figure 3.5: The calculated index of refraction $n(\omega)$ (left) and absorption coefficient $\alpha(\omega)$ (right) of glass from 0.1 THz to 0.35 THz. The refractive index is constant around 2.56. The large absorption of glass at higher THz frequencies prevents the attainment of accurate spectroscopic information for dielectric characteristics above 0.35 THz.

The index of refraction and absorption coefficient $\alpha(\omega)$ of the glass sample used in Section 3.3 is also calculated and plotted in Figure 3.5. The index of refraction of glass is constant at approximately 2.56 from 0.1 THz to 0.35 THz. Due to the depletion of frequencies above 0.35 THz by transmitting through glass, accurate information regarding the index of refraction cannot be determined past 0.35 THz with this method. This large absorption in glass at high frequencies is displayed in the plot of its absorption coefficient in Figure 3.5.

3.3 Dove Prism Reflection Spectroscopy

The UHMW dove prism designed in Section 3.1.2 is used to examine and compare reflections at UHMW-sample interfaces, as well as test the reflection spectroscopy analysis. Figure 3.6 details the alignment of the dove prism. The dove prism is placed between the THz-TDS transmitter (T_x) and receiver (R_x), which are oriented in the TE polarization. It can be noticed that the dove prism acts as an optical black box, returning the THz pulse to its original propagation after one reflection at the interface of interest. This simplifies reflection measurements for different UHMW-sample interfaces by constraining the propagation of the THz pulse to a plane parallel to the mounting table.

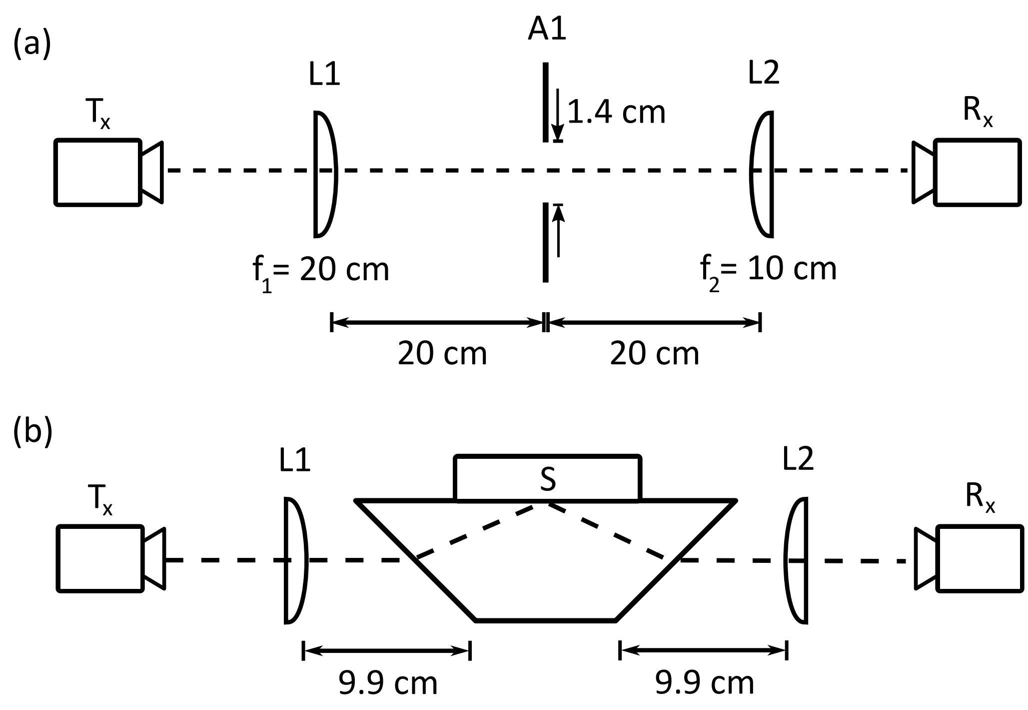

Figure 3.6: (a) Schematic of the THz beam spot measurement. Silicon lenses (L1,L2) have focal lengths, f_1 and f_2, respectively. The aperture (A1) is used to measure the beam spot. (b) Schematic of the dove prism alignment (not to scale). The beam spot is centered on the top face of the dove prism. Dotted lines represent the path of propagation for the detected pulse.

To ensure the measured reflection solely represents the reflection at the interface, the THz pulse is focussed to a beam spot of approximately 1.9 cm by using silicon lenses of focal lengths 200 mm and 100 mm, respectively. The 200 mm focal length lens is required to provide sufficient distance between the lens and the focal point, to ensure the focal point occurs at the top surface of the large dove prism. The latter 100 mm focal length lens is used for a quick focus at the receiver (R_x). Silicon lenses also have a favourable bandwidth in this spectral range consequential of the absence of absorption lines and dispersive effects at THz frequencies [56].

The beam spot is measured with an optical aperture (replacing the dove prism) at a distance approximately the focal length of the lens (200 mm) away from the lens, L1. The diameter of the aperture at which the electric field amplitude of the THz beam drops by $\frac{1}{e}$ of its initial electric field peak (open aperture) gives the beam diameter at the focal point [57]. The electric field amplitude of the THz pulse is directly observed using the T-REX software. Once the THz pulse measurement is located in the time-domain and plotted via the software, the electric field amplitude is displayed. After recording the distances between the lenses (L1,L2) and the focal point (A1), the dove prism is put in place of the aperture, A1. Introducing the dove prism increases the optical path length, so the lenses are brought closer together accordingly such that the focal point is incident with the top face of the dove prism. This minimizes the beam diameter at the reflecting interface of interest. The introduction of the dove prism also leads to an increased time delay of the THz pulse, so the 80 ps time window observing the THz pulse in real-time via the T-REX software must be adjusted to relocate the pulse.

Previously, the beam diameter at the focal point has been measured, but the size of the beam spot projected onto the face of the dove prism needs to be calculated. This gives the approximate size of the surface required to form an acceptable interface with the top face of the UHMW dove prism. Due to the geometrical change of the optical path induced by refraction in the dove prism, the THz beam spot is elongated along the interface by a factor of $\frac{1}{\cos\theta_r} \approx 3.42$, where $\theta_r = 73^\circ$ is the angle of reflection at the interface. For example, assuming an original beam spot of 1.9 cm without the dove prism as discussed above, the elongated beam spot with the introduction of the dove prism is expected to be a factor of 3.42 larger, giving a 6.5 cm focussed beam spot. This helps describe the absolute minimum size of an interface, or the minimum size of a sample in contact with the top face of the UHMW dove prism, to give a reliable reflection.

Once the dove prism is aligned in the TE polarization mode of the THz-TDS optical system, measurements of the electric field of the reflected THz pulse with respect to time can be made. By placing a flat sample on the top face of the dove prism, a UHMW-sample interface is made. These samples consist of varying materials including different metals and wood products, water, air, a stack of paper towel with varying water content, a gold-plated mirror, glass, and other plastics. The first stages of measurements include monitoring qualitative aspects of the reflected THz signal using T-REX computer software for terahertz pulse signal processing and analysis. By resting a sample on the top face of the dove prism, an interface is created with the UHMW, and the real-time signal corresponding to the new reflection is collected. This is repeated for the materials mentioned above. All reflections are compared to the reference UHMW-air interface reflection, for convenience. Contrasting reflections include signal inversions, delays (translations in time), and even entire changes in shape.

Interfaces that produce the most contrasting reflections are then inspected more carefully. Before placing each sample on the dove prism, reference measurements are taken to record the reflection at the UHMW-air interface. Next, a sample is placed on the dove prism in order to record the reflection at each UHMW-sample interface. Reference measurements are of vital importance in this section in order to theoretically predict the reflection from a UHMW-sample interface, and to verify the MATLAB® script written to calculate these predictions based on Fresnel's equations. In Chapter 2.5, Fresnel's equations are used to develop a theoretical model to predict the reflected signal at an interface with a known dielectric function or index of refraction ($\tilde{\epsilon} = \tilde{n}^2$) given only a reference signal from the dove prism. A script has been written in MATLAB® to calculate and plot these predicted signals. It is shown in equation (2.19) that the electric field of a reflection from a UHMW-sample interface $E_{sam}(\omega)$ can be written in terms of Fresnel's reflection coefficients and the electric field of the reflection at a reference interface $E_{ref}(\omega)$ (UHMW-air), provided all other parameters are fixed. The Fast Fourier Transform or Inverse Fast Fourier Transform functions in MATLAB® are used to express the electric fields in either the frequency or time domain, respectively [58]. The measured UHMW-sample reflections are plotted with their corresponding predicted reflections in the interest of testing the model outlined in Chapter 2.5.

These measurements are repeated to align the TM polarization mode of the THz-TDS receiver and transmitter. To obtain a TM polarization, the emitter and receiver heads are rotated by 90°. It is noted that the reflections contrast at a substantially higher degree, in this configuration, thus the interfaces are more distinguishable. This provides motivation to continue the rest of the experiment in this thesis using the TM configuration. Nonetheless, in the remaining sections of this thesis, the TE configuration is employed.

3.3.1 Experimental Results

By following the above procedure, a collection of measured waveforms in the time domain is obtained from UHMW-sample interfaces created by the dove prism and a selection of samples. Reference waveforms (UHMW-air reflections) are recorded immediately following each reflection measurement of a sample on the dove prism.

Samples examined on the dove prism exhibiting contrasting THz reflections among the group include a gold-plated mirror, water, and glass, along with the reference air reflection. Using transmission spectroscopy, the refractive indices for UHMW and glass have been determined. Similar to reflection spectroscopy, the calculation of the index of refraction of a material through transmission spectroscopy relies on reference and sample measurements of a THz pulse. The amplitude and phase changes of the THz pulse due to the introduction of the sample provide information to determine the refractive index and absorption of the sample. Chapter 2.4 details this method used to determine the refractive indices for UHMW and glass as in Section 3.2. The empirical dielectric function of water is calculated using the double Debye model with the parameters discussed by Uhd Jepsen et al. [59]. The empirical dielectric functions of gold and aluminum are calculated using a similar Drude model and parameters presented by Zeman et al. [60].

In order to determine which UHMW-sample interfaces produce contrasting reflections, a qualitative form of spectroscopy in the time-domain is used to directly observe changes in amplitude, delay or shape of the pulse. By plotting THz pulse reflections from each interface in the time-domain (with respect to its time delay), these changes in pulse properties are identified, thus revealing contrasting interfaces to be used in the imaging sample in Section 3.4.

Once the refractive indices or dielectric functions of the samples are determined, the script written in MATLAB® is used to calculate and plot the associated predicted THz pulse reflected from the UHMW-sample interface, given the reference reflection from a UHMW-air interface and an angle of reflection of 73°. Figure 3.7 shows the reflected THz pulse from each UHMW-sample interface of the dove prism for the TE and TM polarizations. The reflected waveforms for each interface examined in the TE polarization appear to differ primarily by amplitude. The lack of substantial changes in shape or form of the reflected pulses suggest minimal phase change upon reflection at these interfaces. It is speculated that distinguishing between four differing interfaces solely by amplitude changes upon reflection may be exceptionally challenging in a more practical setting; in such a setting, fewer parameters of the system can be held fixed.

Upon plotting the reflections from identical interfaces in the TM polarization, the problem outlined above is resolved. Figure 3.7b displays the significant change in shape of every interface examined in the TM polarization. In contrast to the UHMW-air interface, the reflection from the UHMW-gold interface undergoes an inversion of the waveform as well as a small degree of attenuation. The UHMW-water and UHMW-glass reflections are heavily attenuated while displaying some difference in form such as the small peak at approximately 2063 ps exhibited by the UHMW-water reflection. This suggests a common phase shift between the reflections at the two interfaces created by water and glass. Due to these significant qualitative amplitude and phase changes between the differing interfaces, it is suggested that TM polarized reflections are more distinguishable, and the identification of these interfaces concealed by UHMW in a practical setting may be more definitive and efficient using TM polarization rather than TE polarization.

Following the comparison of TE and TM polarization for this system, it is essential to verify the theoretical reflections modelled earlier with the corresponding measured reflections. This allows for a similar model to be used for imaging concealed interfaces in a practical setting in the next section of this thesis. Figure 3.8a shows the measured reflected THz pulses from the interface of the UHMW dove prism and the sample in the TM polarization, once again displaying the distinguishability between each reflection in this mode. Figure 3.8b-d plots, side-by-side, the measured and predicted reflected THz pulses from a UHMW-glass, UHMW-gold, and UHMW-water interface of the dove prism. The predicted reflections for the UHMW-glass and UHMW-water interfaces agree with the measured wave-

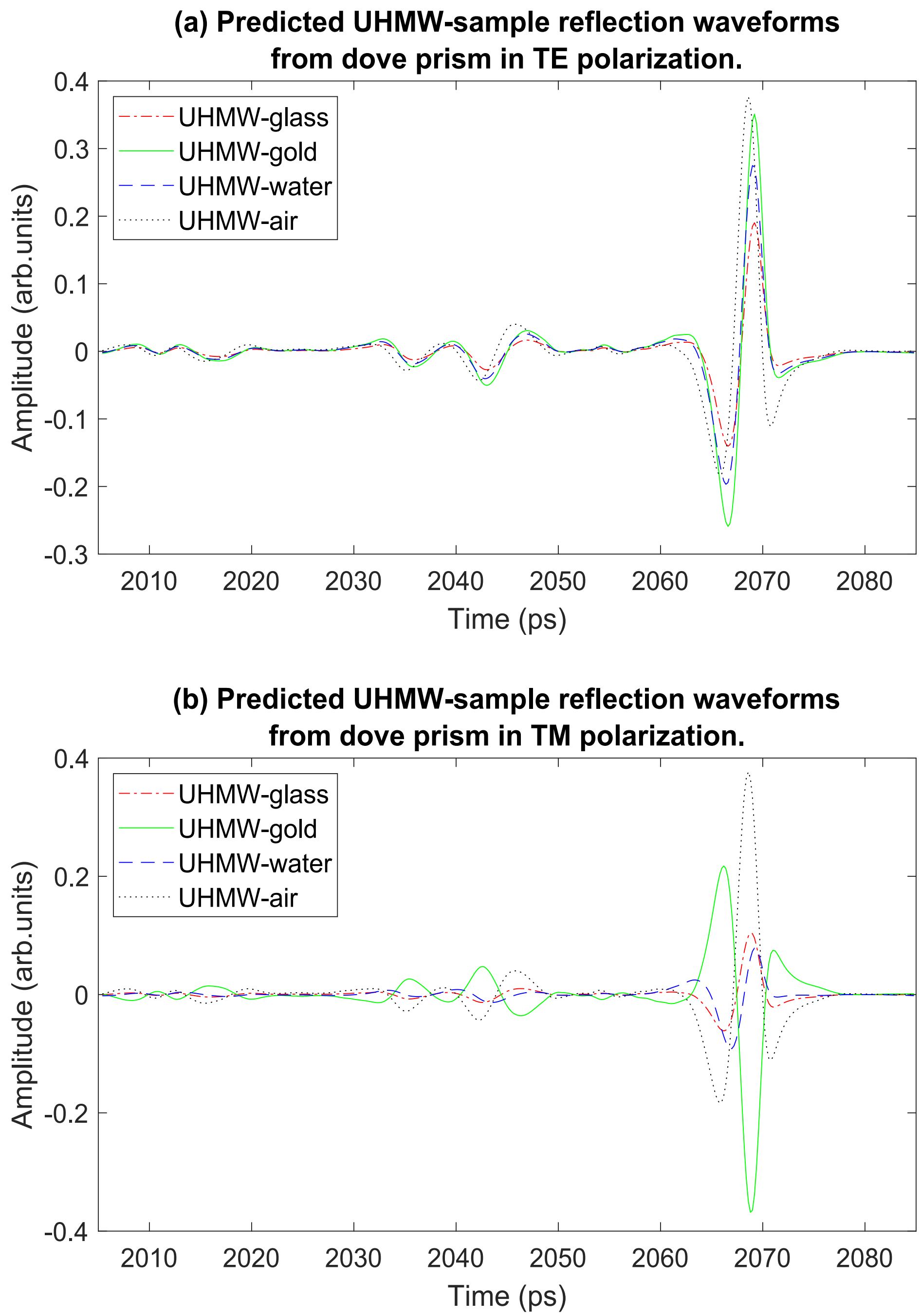

Figure 3.7: Predicted THz waveforms output by the UHMW dove prism system with a reflecting UHMW-sample interface, using (a) TE and (b) TM polarizations. Given one reference measurement (UHMW-air) for each configuration, reflections at other UHMW interfaces are calculated.

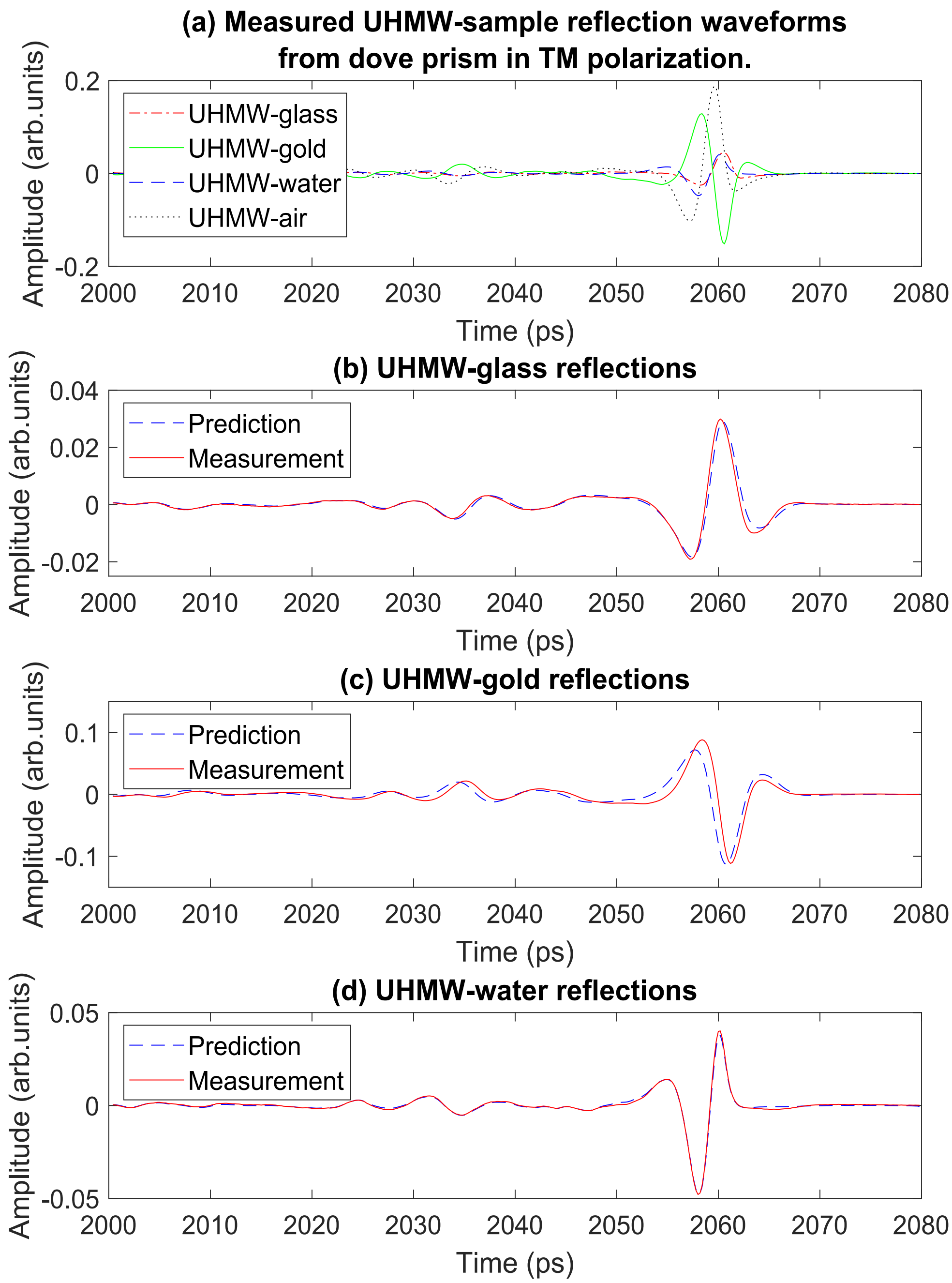

Figure 3.8: (a) Measured THz waveforms output by the UHMW dove prism system with a reflecting UHMW-sample interface (TM polarization). Predicted and measured THz waveforms output by the dove prism from a (b) UHMW-glass interface, (c) UHMW-gold interface, (d) UHMW-water interface (TM polarization).

forms.

The measured reflection for the UHMW-gold interface does not have as strong an agreement with the predicted reflection as compared to the other interfaces, however, both of these measured and predicted waveforms are of similar form and are distinguishable among the reflections plotted in Figure 3.8. This weak agreement can be explained by the nature of the sample used for the UHMW-gold interface. Firstly, a 76.2 mm protected gold mirror is used for the gold sample, which is the largest one available. The dielectric overcoat on the gold-plating of the mirror may have reduced the quality of the UHMW-gold interface, however typical thicknesses for these coatings are well below the order of magnitude of the wavelength of THz radiation, so its measurable effect in this configuration is unlikely [61].

The factor that is most likely diminishing the quality of the UHMW-gold interface is the size of the mirror. Earlier in this section, an expected focussed beam size incident at the top surface of the dove prism has been estimated. When constructing a sample for forming an interface with UHMW, it is favourable to select dimensions that considerably exceed the beam spot size since the electric field amplitude is $\frac{1}{e}$ of its initial maximum at the beam waist. This ensures that a large fraction of the incident electric field reflects from the supposed interface. Because the beam spot (6.5 cm) and gold mirror diameter (7.62 cm) are close, it is suspected that the entire THz pulse does not reflect at the designated UHMW-gold interface. Other samples used throughout this section are also substantially larger than the beam spot, explaining the better agreements with theory of the other reflections.

To verify the speculation above, Figure 3.9 displays the contrast in the agreement with theory between the reflections from the UHMW interfaces with the small gold sample and the larger aluminum sample. The reflection from the sufficiently large sample (aluminum) agrees with theory, while the reflection from the gold sample is not a perfect match with the predicted pulse. It can be noted that the predicted reflected pulse from both metal samples are identical, illustrating the expected reflection from any sample possessing an extreme dielectric contrast to UHMW.

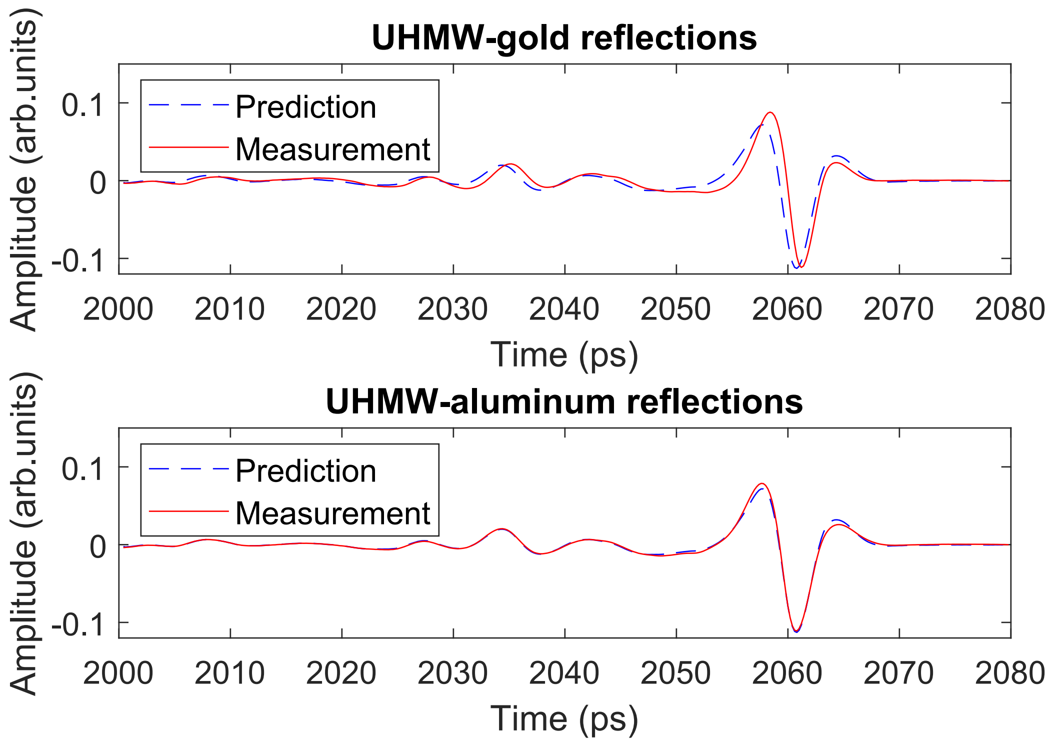

Figure 3.9: Predicted and measured THz waveforms output by the dove prism from a UHMW-gold interface (top) and UHMW-aluminum interface (bottom). The aluminum sample is larger than the gold sample, thus reflecting a greater amount of the THz pulse, and strengthening the agreement with theory.

Nonetheless, the reflection spectroscopy model written earlier supports the measured reflections at each interface. The four samples that have been examined in this section also provide identifiable and distinguishable reflections at THz frequencies for each respective UHMW-sample interface.

Also, for measurements in the TM mode, the force exerted on the sample affects the measured reflection. The greater the force is on the sample creating the interface with the dove prism, the better the agreement is between the predicted and measured reflections. This is not the case for the TE mode since the force exerted on the sample does not significantly affect the measured reflection. This reduction of accuracy for measurements in the TM mode can be explained by the considerable contrast between UHMW-air interface reflections and other interface reflections within the imaging sample, exclusively during operation in the TM mode, as seen in Figure 3.7. It is expected that interfaces in practical systems are not perfect interfaces whereas the intrusion of small air gaps between two media may be present. In this case, a small portion of the THz pulse reflects as if the interface was a UHMW-air interface, affecting the detected waveform by the combination of contrasting reflections. In the TE mode, where the UHMW-air interface reflection is identical in form (but not amplitude) to the other interface reflections, small air gaps at the interfaces may not be easily detectable due to the lesser degree of contrast of its reflection, as opposed to the TM mode. By exerting a force on the sample, small air gaps are mostly eradicated, but still may have affected accuracy in the measurements seen in Figure 3.8.

3.4 THz Reflection Imaging

After validation of the reflection model for a UHMW system involving varying interfaces, a THz reflection imaging system must be set up and aligned in order to explore the possibility of spatially locating and identifying materials concealed within a UHMW layered system in an applied setting. A similar imaging apparatus to the Brewster's angle reflection imaging system designed by Kilcullen et al. is used [19]. Figure 3.10 is a labelled photograph of the reflection imaging system in operation. Figure 3.11 displays the THz pulse path of propagation throughout the imaging system. The entire system is aligned optically, using a mounted green laser pointer.

In order to align all four mirrors and sample with the transmitter (T_x) and receiver (R_x) heads, the imaging sample is replaced with a flat gold-plated mirror (S). For the purpose of suspending the mirrors in such a way that the incident horizontal THz pulses from the transmitter are directed downwards onto the imaging sample and allowing the sample to be translated in space below the mounting system, all four mirrors are mounted onto a raised crosspiece constructed from four stacked dovetail rails. For sufficient clearance of the apparatus above the imaging sample plane, on each side of the rail crosspiece, one pillar post is attached beneath a post holder and post, which is ultimately attached to the crosspiece. The post holder allows for height adjustments of the entire reflection apparatus.

Next, two gold-plated parabolic mirrors (PM1 and PM2) are mounted against the underside of the rail crosspiece to focus horizontally incident light vertically downwards. By mounting a pair of gold-plated flat mirrors (M1 and M2) directly below the parabolic mirrors, the focussed light is redirected downwards and towards the center of the table. The flat mirrors are angled and positioned such that the focal point lands below the lowest mirrors, centered above the table and at the imaging sample plane (S). It is important for the focal point of the propagating

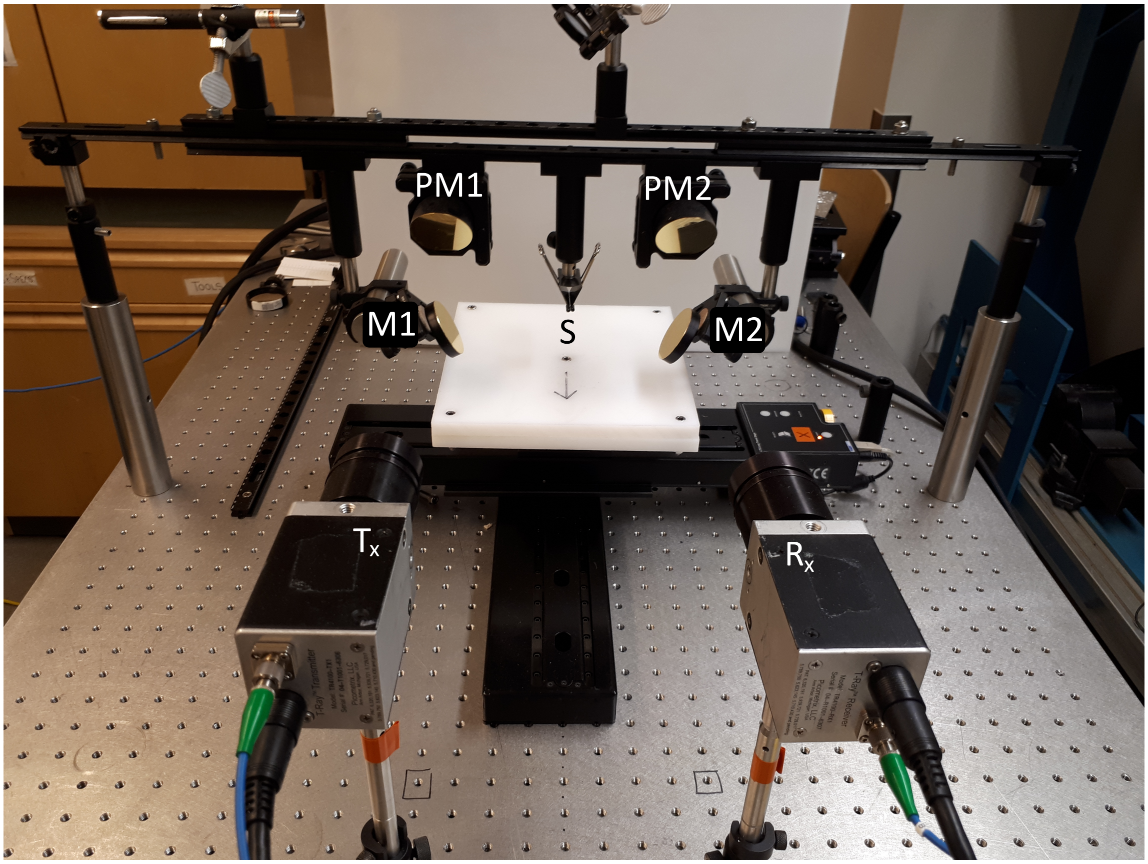

Figure 3.10: The complete reflection imaging system used to raster scan the imaging sample at a selected depth. [T_x - transmitter, R_x - receiver, PM1/PM2 - parabolic mirrors, M1/M2 - flat mirrors, S - imaging sample.]

light to be centered because the reflected focussed light from the sample is then redirected and collimated towards the receiver by the flat and parabolic mirrors on the opposing side of the apparatus. In this way, the symmetry of the apparatus and of the path of propagation of the incident THz pulses dictates the quality of the imaging measurements. The gold mirror in place of the imaging sample (S) for alignment is mounted on a mechanical jack to adjust its height. After raising this gold mirror to a top surface height of 14.5 cm above the table, the reflected THz pulses are successfully collimated into the receiver head. At this height, the detected THz pulse, which is monitored via the T-REX software, is at its strongest. The angle of reflection at the surface of the gold mirror in place of the sample is

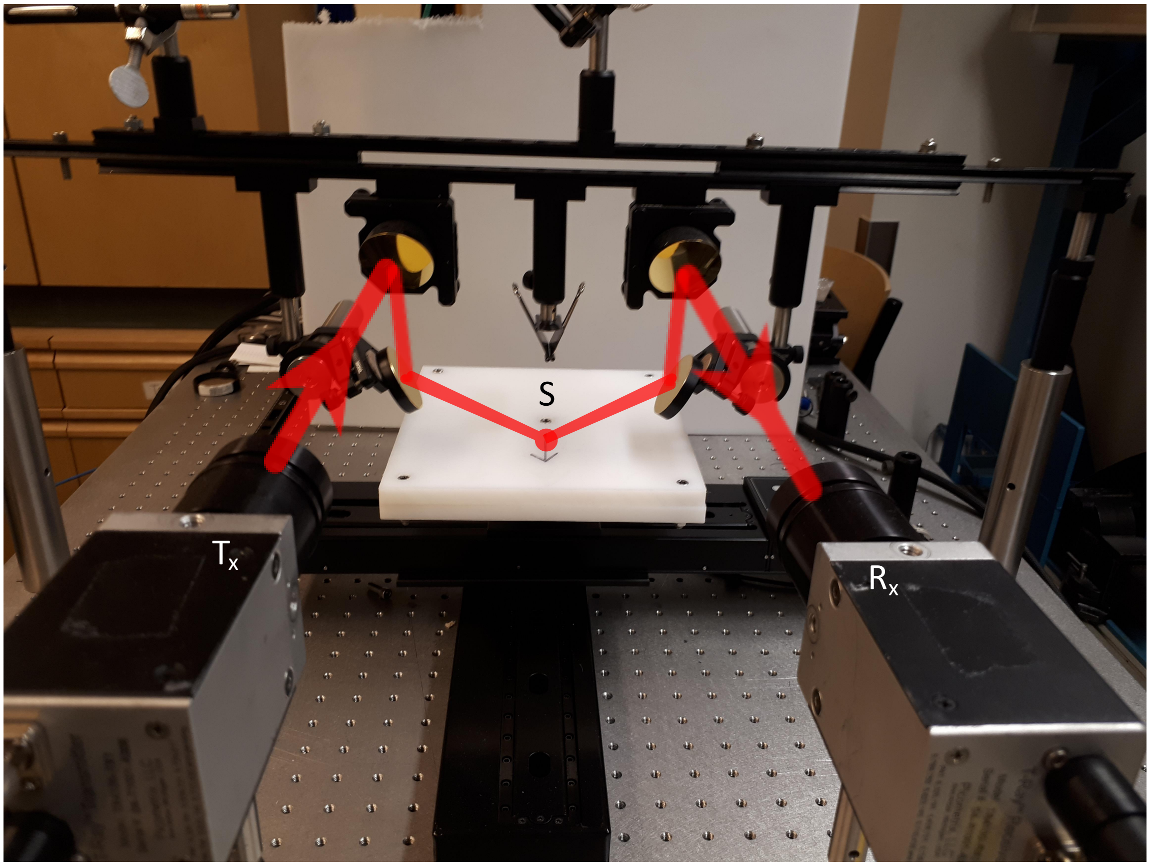

Figure 3.11: The path that a measured THz pulse propagates through the reflection imaging system. [T_x - transmitter head, R_x - receiver head, S - imaging sample.]

approximately 60°.

Following the construction and alignment of the reflection measurement apparatus, the optimal height of the imaging sample above the mounting table needs to be determined. By inspecting concealed interfaces underneath the top layer of the imaging sample, a change in the path of propagation by refraction of the THz pulses is introduced as compared to a direct reflection from air to the gold mirror. This requires the top surface of the imaging sample to be raised a height, Δh, higher than the original focal point height in air of 14.5 cm. This change in height is calculated in the following equation utilizing the geometry of the paths of light in air as well as the refracted path through the top layer of the imaging sample:

$$\Delta h = \frac{d\cos\theta}{\sqrt{n^2 - \sin^2\theta}}. \tag{3.1}$$

Given the thickness of the top layer of the UHMW imaging sample (d=1.27 cm), the refractive index of UHMW (n=1.52), and the angle of incidence at the top surface (θ=60°), the surface of the imaging sample must be raised by about 0.5 cm above the focal point in air.

After this calculation, the mechanical jack used to mount the imaging sample is adjusted such that the top surface of the imaging sample is 15.0 cm above the mounting table. All reflection measurements in the remainder of this thesis are collected with the surface of the imaging sample at this height. Only precise lateral translations of the imaging sample are to be executed for imaging purposes. Now that the focal point of the THz pulses occur at the first interface below the surface of the imaging sample, the output THz pulses that are detected from the reflection imaging system contain accurate information regarding the properties of that concealed interface. By analyzing these reflections, spatial and material properties of the interfaces concealed within the sample can be determined.

3.4.1 Automation of the Image Measurements

In order to automate the reflection measurements for imaging purposes, two motorized translation stages are mounted beneath the imaging sample and perpendicular to each other. This allows for precise positioning of the imaging sample for automated measurements of a reflected THz pulse to construct an accurate spatial image. Using a USB cable, the motorized translation stages contain integrated electronic controllers that are controlled by a computer via Thorlabs' APT™ software. MATLAB® scripts, in combination with macros, have been written to control the

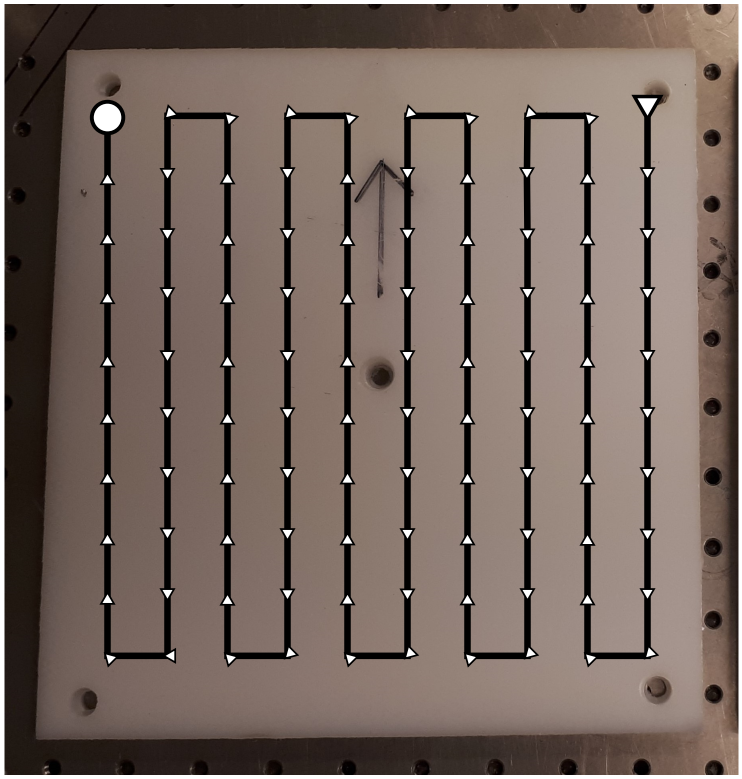

Figure 3.12: An illustration of the incremental positions of the imaging sample within the reflection imaging system for a 10 by 10 raster scan. The starting position, (X_i, Y_i), is given by the large white triangle, the finishing position, (X_f, Y_f), is given by the large white circle, and directions are indicated.

APT™ and T-REX software in order to laterally position the imaging sample and to collect THz pulse data at that position, respectively. To obtain a spatial image of the concealed interfaces within the imaging sample, imaging measurements are obtained in the form of a raster scan. After centering the top-right corner of the imaging sample under the reflection imaging system, the positions of the translation stages are recorded as (X_i,Y_i). This is repeated for the bottom-left corner of the imaging sample, recording (X_f,Y_f). For an image of a desired resolution, m by n, the incremental position changes are given by $\frac{X_f - X_i}{m}$ and $\frac{Y_f - Y_i}{n}$. The imaging sample is scanned using these positional increments in order to consistently space the reflection measurements over the entire sample to create an m by n depth image of the interfaces within the sample. Figure 3.12 illustrates the starting and finishing points of an example raster scan as well as the incremental positions of the sample which is kept stationary for the duration of each measurement. Following the scan, in-depth analysis algorithms written in MATLAB® are used to spatially plot the amplitude and phase, as well as other spectroscopic features, of the measured THz pulses for these images.

Following the construction of the reflection imaging apparatus, it is observed that a front reflection from the top surface of the imaging sample interferes with the reflection measurements of the subsurface interface of interest. This small air-UHMW reflection occurs approximately 100 ps before the measured reflection, introducing noise within the system. The original design of this imaging system is intended to minimize these front reflections by operating near Brewster's angle as the angle of reflection of the first UHMW-air interface at the top of the imaging sample (approximately 60°) [62]. The front surface back reflection is only reduced for the TM polarization. As a result, for TE polarization, front surface back reflections need to be minimized using a beam block to improve signal quality. In order to prevent this signal interference, a front reflection blocker is constructed from a thin, flat strip of aluminum foil. It is mounted and centered directly above the imaging sample, as close as possible to its top surface without impeding motion of the sample during imaging. The introduction of this front reflection blocker successfully diminishes the amplitude of the top reflection such that the addition of the signal is negligible to the reflection from the concealed interface.

3.4.2 Preparation of the Concealed Samples

Before imaging of the concealed interfaces inside the UHMW imaging sample is performed, three different samples are prepared for containment in each of the milled 3.2 cm square sections of the bottom layer of the imaging sample. In Section 3.3 reflections from various interfaces are examined by use of the UHMW dove

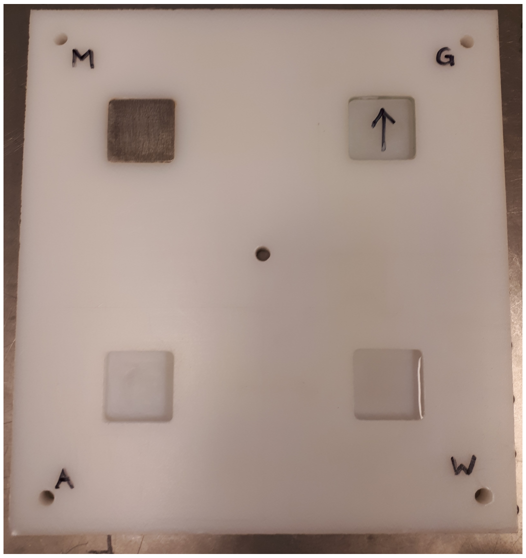

(a) Bottom layer of imaging sample.

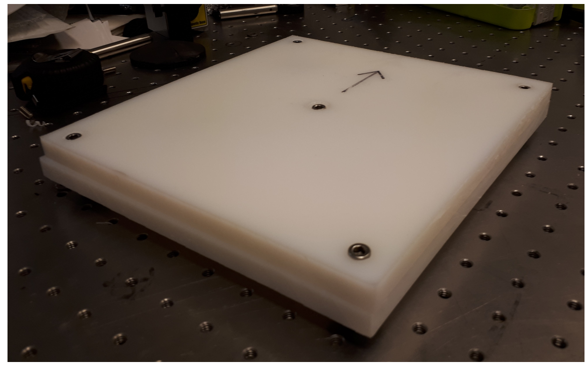

(b) Complete imaging sample.

Figure 3.13: A photograph of (a) the bottom layer of the imaging sample with sample inserts and (b) the imaging sample fully enclosing the sample inserts. The top-left section (M) contains steel, the top-right section (G) contains glass, the bottom-left section (A) contains air, and the bottom-right section (W) contains water.

prism. Based on the substantial qualitative contrast of the reflections from the gold-mirror, glass, water, and air, all but one of these materials are selected as a sample insert.

Figure 3.13a illustrates the corresponding location for each sample insert inside the imaging sample. The reference air sample requires minimal preparation since an empty square section within the imaging sample creates the desired UHMW-air interface. The glass sample is prepared by cutting a 3.2 cm square from a 0.64 cm thick glass sheet. The edges are carefully sanded to a flush fit into one of the milled sections of the imaging sample. In place of the gold sample, a 3.2 cm steel sample is cut from steel flat bar using an angle grinder. This significantly minimizes the cost of the materials while the conducting, metallic properties of the sample insert remains sufficient for the aim of this experiment. The steel sample is filed and polished to a flush fit into a milled section of the imaging sample.

The final sample consists of tap water. A glass pipette is used to fill its corresponding section to the desired amount. One issue that continuously arises in this part of the experiment is the problematic leaking of water into other regions of the imaging sample. The intrusion of water into other regions of the imaging sample is detrimental to the integrity of the surrounding reflection measurements. In order to minimize the intrusion of water from its designated section, a 3.2 cm square absorption inlay constructed by numerous square paper towels of a similar size is used to fill the milled section to absorb and contain the water within its assigned section. Water is then added until the section is full. The optimal thickness of the absorption inlay is such that without force or contact, the water-saturated absorber slightly overfills the pocket. Upon contact with the top layer of the imaging sample for concealment, the saturated absorber is slightly compressed until flush with the interface, thus releasing a small amount of water to create the UHMW-water interface. It is crucial to add the optimal amount of water to ensure the surfacing of water upon compression of the absorber, but not such an amount that may lead to the leakage of water into other regions.

The approach to the containment of water in this thesis requires the acknowledgment that the interface created by the saturated absorber may not be identical to the interface that is created by only water. There is a large contrast, however, between the dielectric properties of water and paper that leads to the following assumption. First, the absorbing properties of water are large enough to completely prevent the transmission of THz radiation through a single damp paper towel [63]. Second, paper towels, which make up the absorber, are nearly transparent at THz frequencies, thus speculations on principles from effective medium theory indicate that the medium resulting from the combination of water and paper towels respond almost identically to a water medium, with respect to its optical properties [64].

3.4.3 Experimental Results

After bolting together the top and bottom layers of the imaging sample, the completed sample with various concealed interfaces is imaged as detailed in Section 3.4.1. After acquiring the time-domain measurements representing the electric field of the reflected THz pulses for a 100 by 100 image, the collection of reflection measurements must be analyzed in order to construct spatial images, which represents the spatial distribution of the amplitude and phase of the reflected THz pulses. To quickly summarize, first, a base THz image must be constructed, which accurately represents the spatial features of the concealed interface within the layered system. Subsequently, an in-depth analysis of the THz waveforms is used to inspect the 100 by 100 image data, thus determining specific properties of the THz reflections that are unique to a given interface. For example, the UHMW-metal interface is expected to be highly reflective due to the large dielectric contrast and conductivity of metallic objects, suggesting a substantial reflecting amplitude from this interface, which may be a unique property for identification among the other concealed interfaces. Using these properties, interface-specific image filters are designed in MATLAB®, which are used to create a 'filtered' copy of the original, base image for each interface. Each interface-specific filter overlays a different set of coloured pixels on a spatial THz reflection image of the concealed interfaces, identifying the spatial distribution of each interface by its analogous pixel colour.

The first phase of interpreting the THz reflection image data involves mathematically inverting the domain of the data points by use of the fast-Fourier transform. Figure 3.14 compares the electric field $E(t)$ of the THz pulse in the time-domain with the complex amplitude of the same electric field $|\tilde{E}(\omega)|$ in the frequency domain for each concealed interface. Since the transformation of the electric field to the frequency-domain yields a complex-valued function, it is commonly visualized by plotting the complex amplitude. In this form, the variation

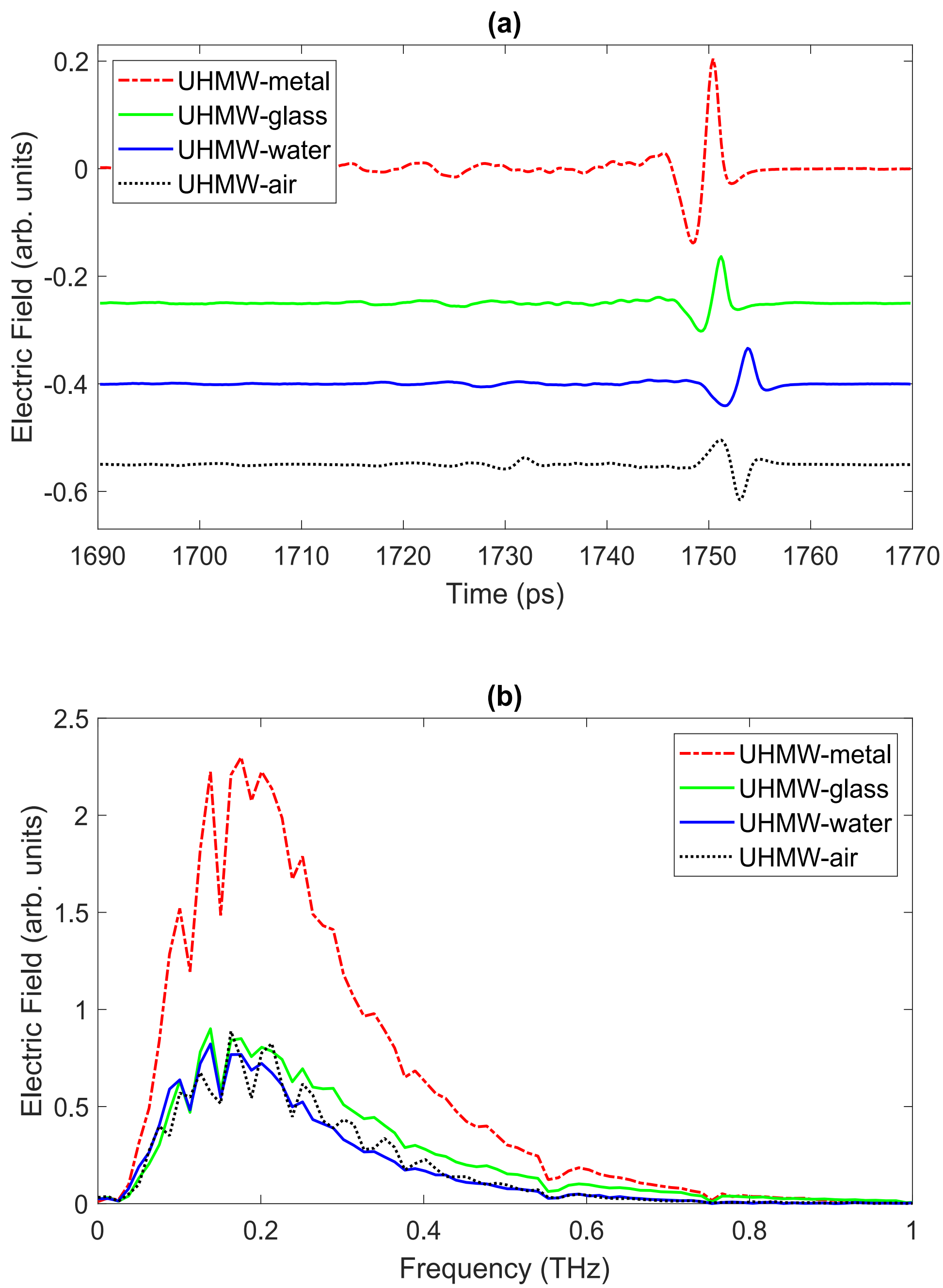

Figure 3.14: (a) Detected time-domain THz pulses reflected from the imaging sample with different interfaces. (b) The amplitude of the fast-Fourier transform, $|\tilde{E}(\omega)|$, of each detected pulse.

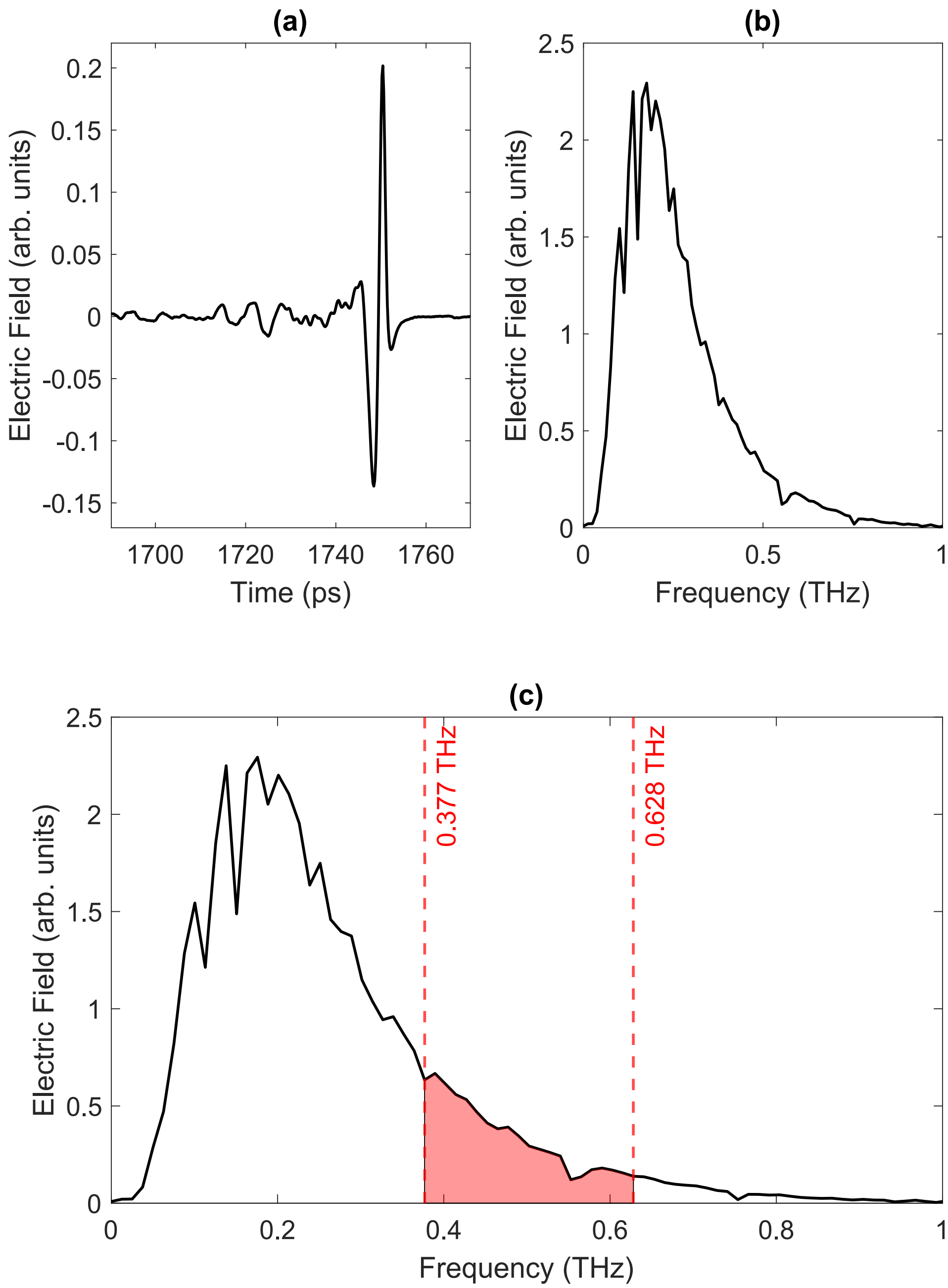

Figure 3.15: A brief outline for calculating pixel intensity values for the amplitude image. (a) The time-domain THz pulse undergoes a fast-Fourier transform to give $\tilde{E}(\omega)$, which is shown in (b) as $|\tilde{E}(\omega)|$. (c) This curve is integrated over 0.377 THz to 0.628 THz to obtain the pixel value at the spatial location of the corresponding reflection.

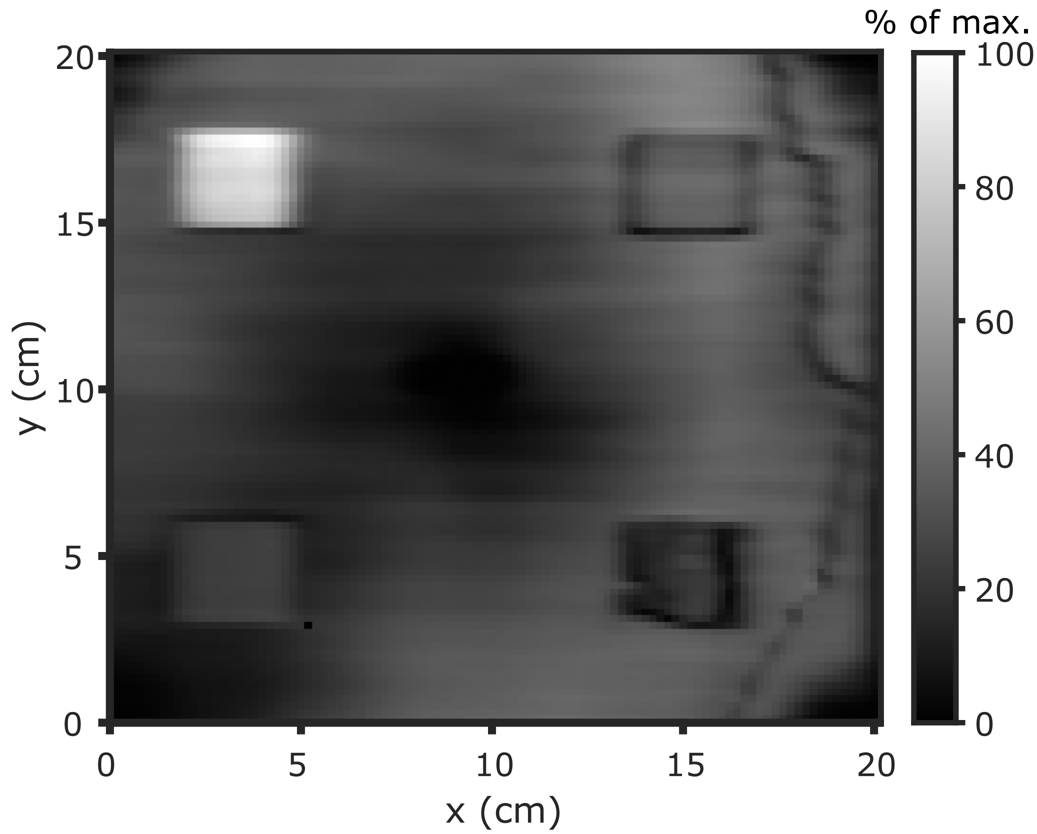

Figure 3.16: A 100 by 100 amplitude image of the concealed interfaces within the imaging sample. The pixel intensities represent the amplitude of the reflected electric field. These values are averaged over the frequency range 0.377 THz to 0.628 THz.

of the electric field amplitude with respect to each frequency can be observed. By selecting a frequency, a single value is obtained for each reflection measurement, indicating the amplitude of the electric field detected for that frequency. By repeating this for each spatial measurement of the amplitude, an image containing the electric field amplitudes at the selected frequency as pixel values is constructed. For the purpose of creating an initial image which accurately depicts the structure and locations of the concealed interfaces, the sum of amplitudes is calculated over a frequency interval and used as the pixel intensity of the image. This is similar to integrating the electric field $|\tilde{E}(\omega)|$ over a range of frequencies to reduce noise in the image. Figure 3.15 provides a detailed summary of the results of each step involved in determining each pixel value for an amplitude image integrated from 0.377 THz to 0.628 THz. The resulting integrated amplitude image is presented in Figure 3.16.

With an image constructed that conveys spectral amplitude information from a range of frequencies, the spectral phase information from the measured THz pulses is yet to be investigated. Given complex electric field values from Euler's formula, $\tilde{E}(\omega) = |\tilde{E}(\omega)|e^{i\phi(\omega)}$, the phase of the electric field of a THz pulse is calculated by taking the argument of each complex data point, $\phi(\omega) = arg[\tilde{E}(\omega)]$. The phase $\phi(\omega)$ uniformly increases with frequency, but when the phase rises above π, the value immediately jumps to $-\pi$ and continues its growth ($\phi(\omega)$ is naturally restricted to a range of $[-\pi, \pi]$). Because of this, the phase data is difficult to analyze and various frequencies return identical phase values, which is not physically accurate. The use of the *unwrap* function in MATLAB® vertically translates the remaining phase values by 2π, following each drop in the phase data. The unwrapped phase data consists of a set of values linearly increasing with frequency.

Due to high noise levels on each end of the bandwidth of the THz pulses, phase values at frequencies less than 0.07 THz are cropped prior to unwrapping the

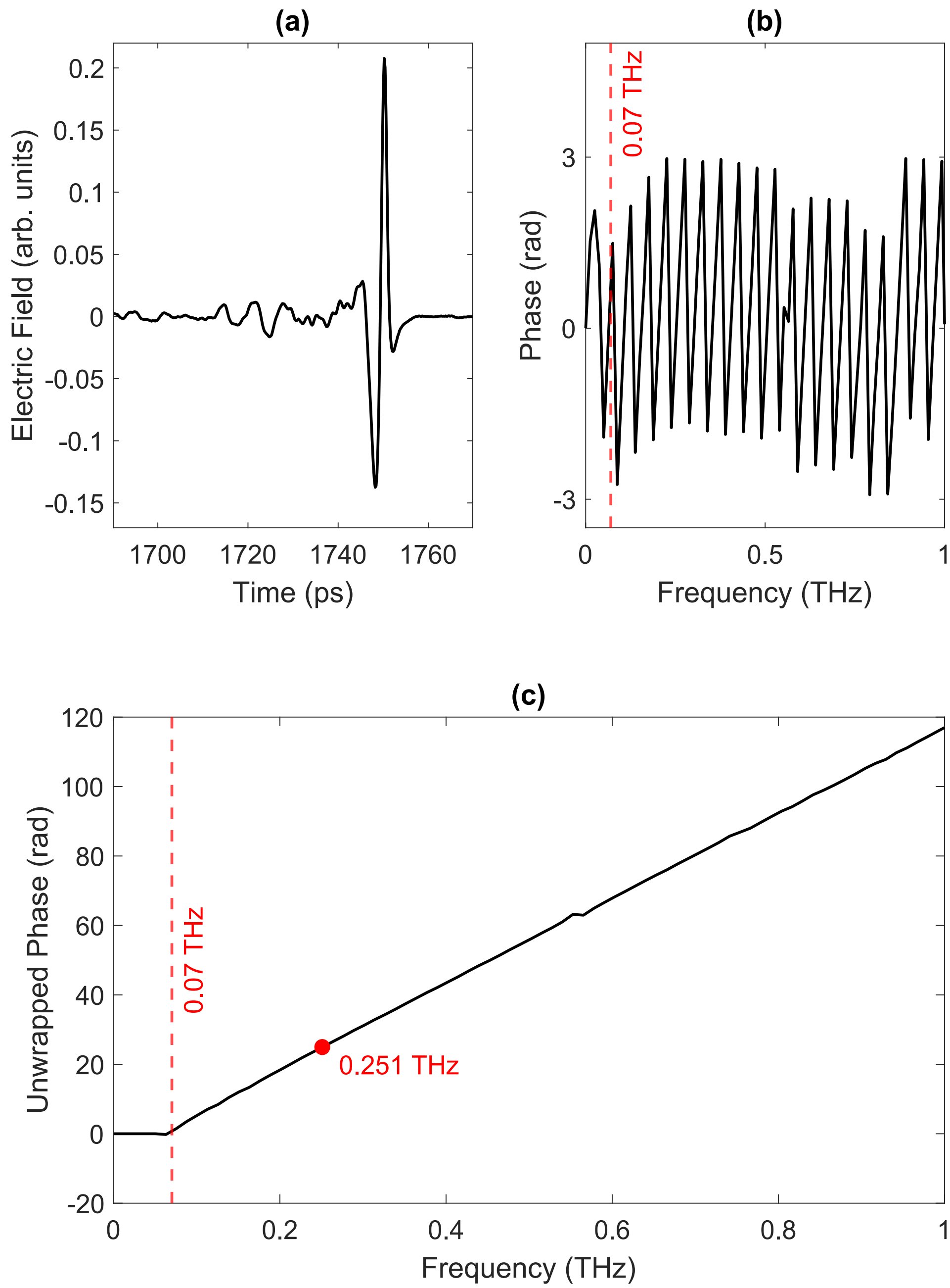

Figure 3.17: A brief outline of a single pixel intensity calculation for the phase image. The measured time-domain THz pulse is displayed in (a). (b) The phase is determined by calculating $\arg(\tilde{E}(\omega))$. To limit effects of noise, only phase data past 0.07 THz is unwrapped to give the trend in (c). The phase value at 0.251 THz gives the pixel intensity for the measured pulse.

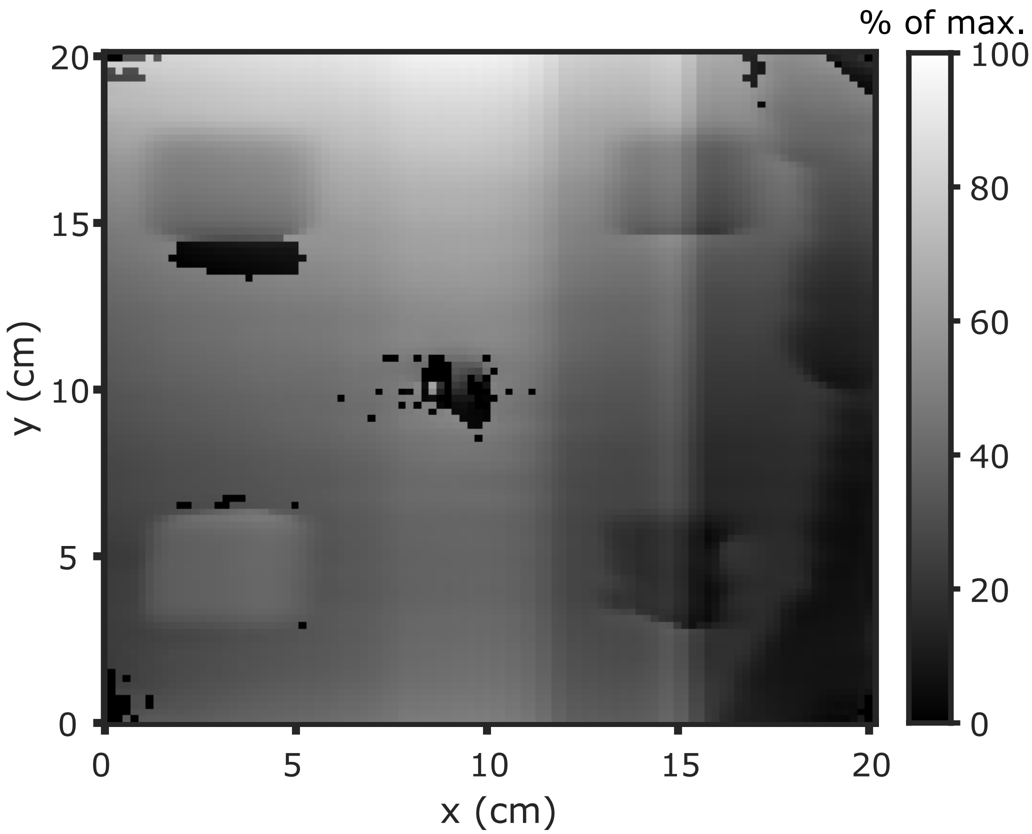

Figure 3.18: A 100 by 100 phase image of the concealed interfaces within the imaging sample. The pixel intensities represent the phase of the reflected electric field at 0.251 THz.

phase. With the extracted phase of the electric fields at each frequency, a phase image can be constructed at a chosen frequency. Figure 3.17 reveals the calculated phase plots (both original and unwrapped phases) used to produce a spatial image of the phase distribution of the THz pulses reflected from concealed interfaces within the imaging sample. Phase values at 0.251 THz are designated as pixel intensities for the phase image exhibited in Figure 3.18.

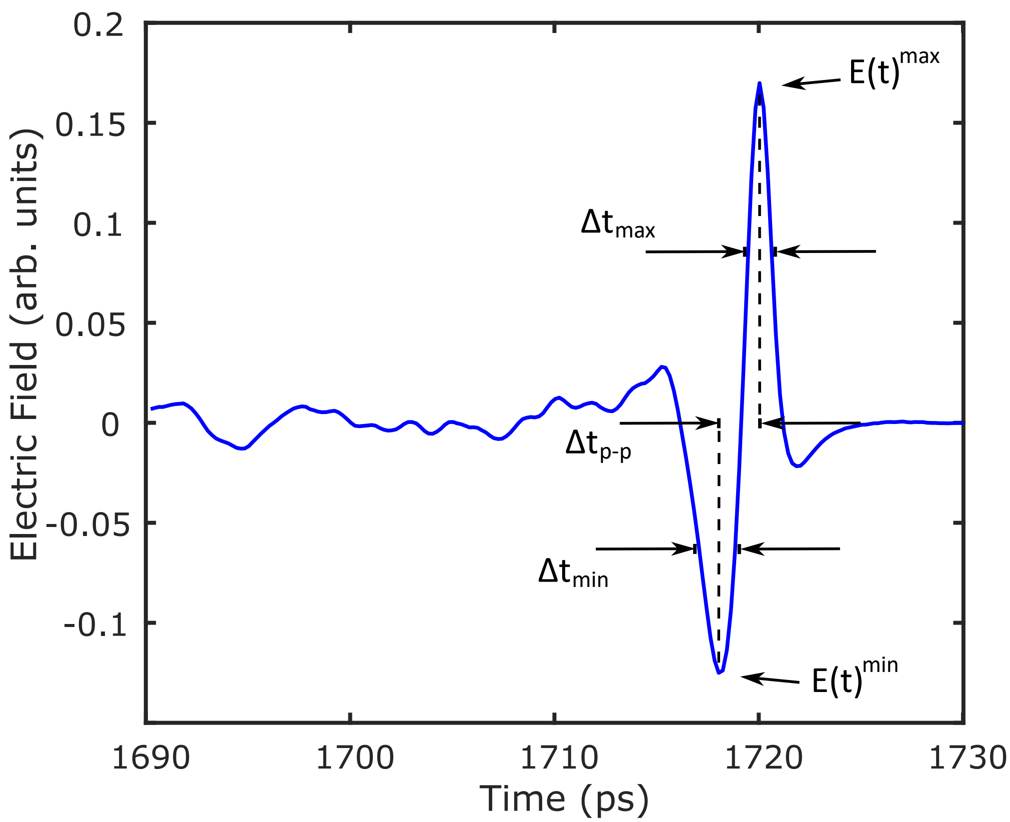

Figure 3.19: A collection of THz pulse characteristics used to create multiple spatial images of concealed interfaces. Features include the maximum and minimum electric field $E(t)^{max}$ and $E(t)^{min}$, peak-to-peak (maximum peak to minimum peak time point) time-width of the pulse Δt_{p-p}, FWHM on either side of $[E(t) = 0]$ Δt_{max} and Δt_{min}.

After testing the analysis of the amplitude and phase of the reflected electric field measurements by creating spatial images illustrating the distribution of the corresponding values, a closer look at the characteristics of a reflected THz pulse is required to differentiate between the concealed interfaces. Figure 3.19 reveals several quantities which can be used to help summarize a THz pulse. Variations in these characteristic quantities are analyzed to develop a collection of features specific to one interface, for the purpose of distinguishing each concealed interface from the rest. Some of the features of the THz pulse include the maximum and minimum value of the electric field in time $E(t)^{max}$ and $E(t)^{min}$, the time-width of the pulse from peak-to-peak Δt_{p-p}, and the time-width of the pulse given by the full width at half maximum (FWHM) on either side of the time axis $[E(t) = 0]$ given by Δt_{max} and Δt_{min}. There are also two other features of interest, which are determined by expanding the analysis of the phase data of the electric field. An additional step is added following the unwrapping of the phase data, which consists of fitting a line to the unwrapped phase data and extracting the corresponding slope (phase shift) m_ϕ and y-intercept (phase offset) ϕ_o. By fitting a line to the phase data, the expected noise introduced into the phase data (due to its high sensitivity to changes in position or thickness) is reduced. The entirety of the previously mentioned THz pulse characteristics are quantified and each trait is used as a pixel intensity for its corresponding spatial image. A diverse selection of THz pulse traits is intended to give multiple dissimilar images displaying different aspects of its spectroscopic information. The collection of images fabricated by these quantities is organized throughout Figures 3.20 and 3.21. It is noted that in Figure 3.20a, the base image produced above from integrating the amplitude from 0.377 THz to 0.628 THz is shown again, for comparison.

The collection of images given by the quantification of numerous THz pulse characteristics allows for the assignment of conditions unique to each interface that establish the image filters for each concealed interface. Specific ranges of values, unique to a given interface, for each quantified characteristic of a THz pulse

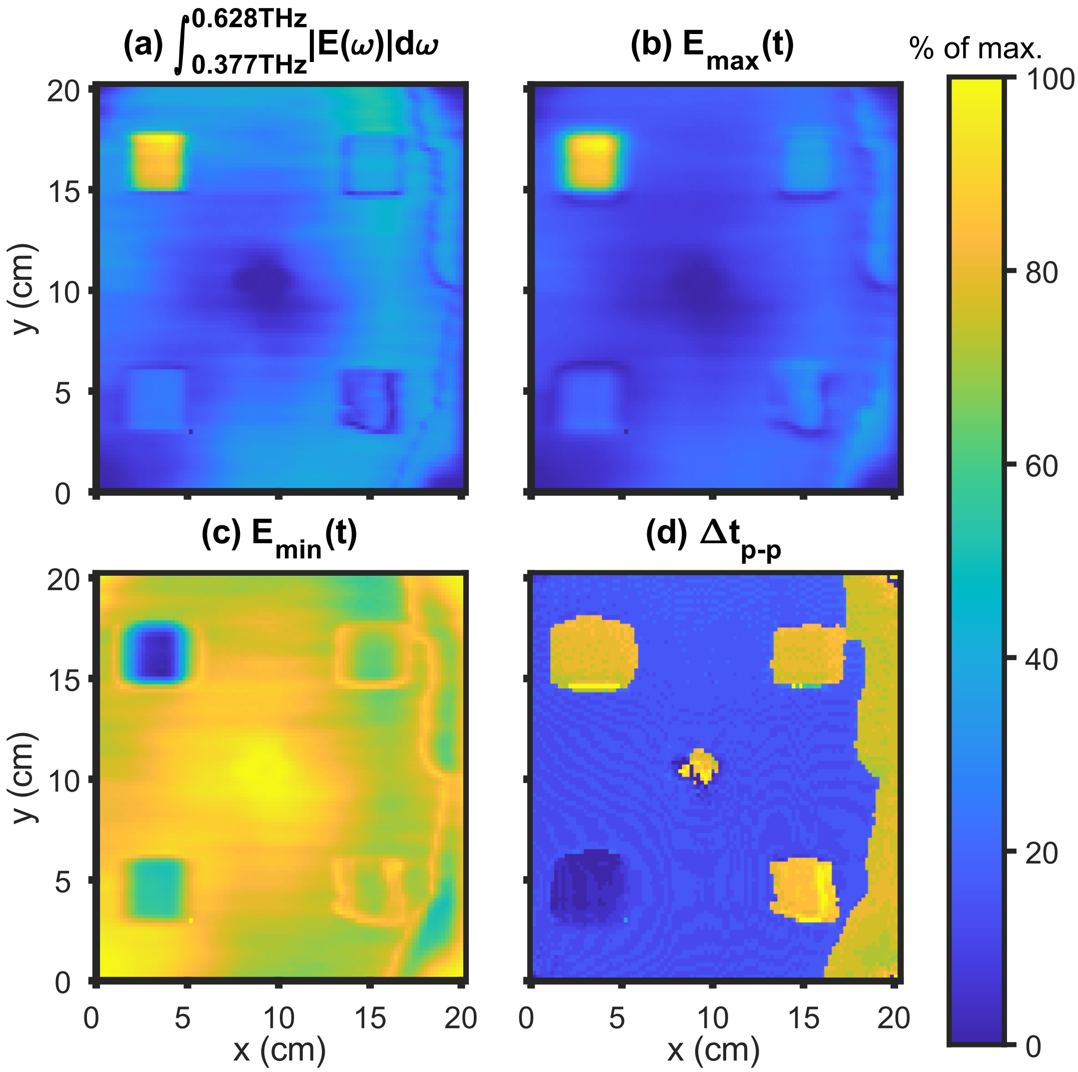

Figure 3.20: A collection of 100 by 100 spatial images with pixel intensities dictated by (a) the integrated electric field amplitude from 0.377 THz to 0.628 THz, (b) the maximum and (c) minimum value of $E(t)$, and (d) the peak-to-peak time-width of the electric field pulse Δt_{p-p}. For convenience and ease in comparison, the colormap ranges from the minimum (blue) to maximum (yellow) pixel value of each image; the centre and corner regions are ignored in this range, since extreme noise values are expected here (where the imaging sample is bolted).

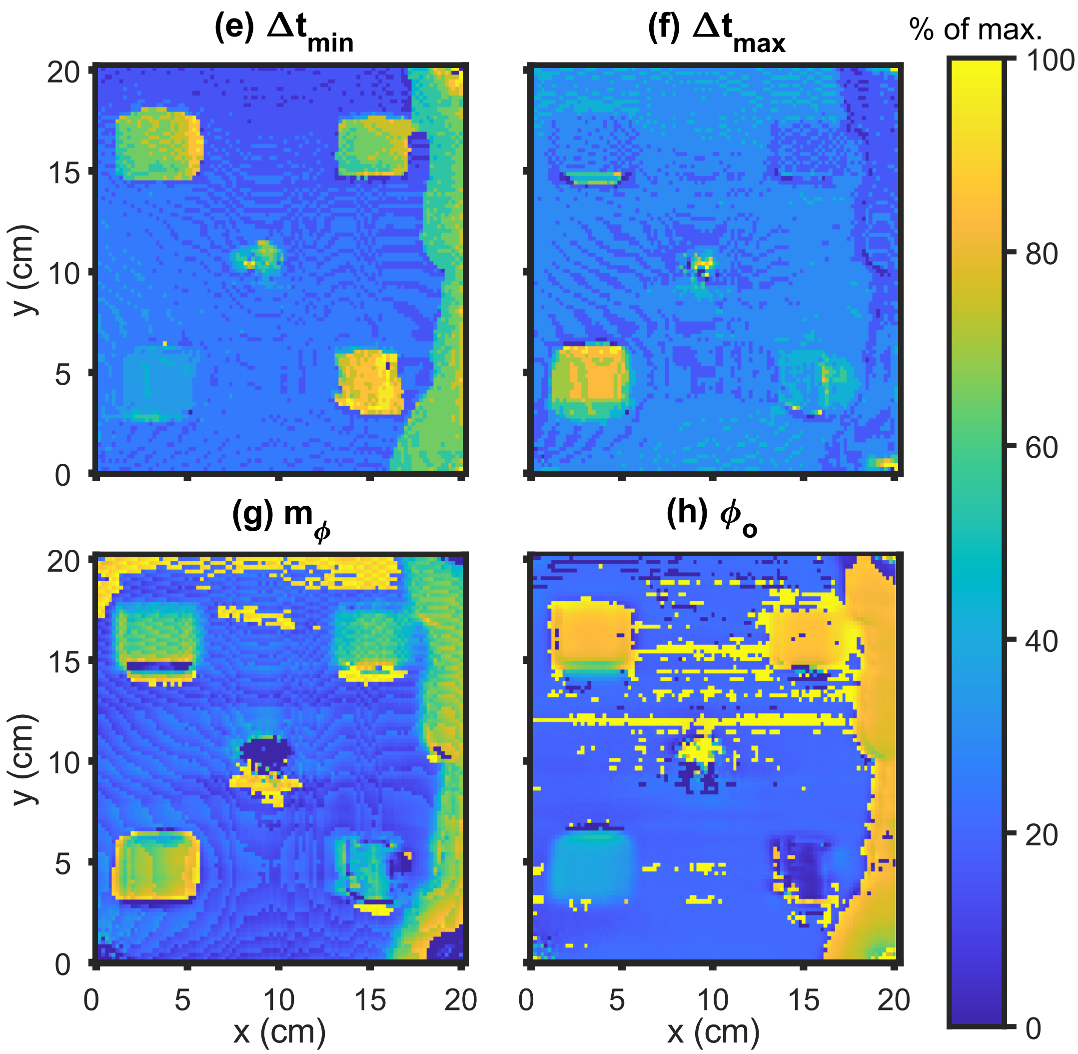

Figure 3.21: A collection of 100 by 100 spatial images with pixel intensities dictated by (a),(b) the FWHM on either side of $[E(t) = 0]$ given by Δt_{min} and Δt_{max}, (c) the slope of the phase data (phase shift) m_ϕ, and (d) the y-intercept of the fitted line to the phase data (phase offset) ϕ_o. For convenience and ease in comparison, the colormap ranges from the minimum (blue) to maximum (yellow) pixel value of each image; the centre and corner regions are ignored in this range, since extreme noise values are expected here (where the imaging sample is bolted).

are carefully applied to each interface in order to identify a concealed interface throughout the reflection image. An image filter for each interface is built by designating passing conditions, of which all were required to succeed, to identify a given measurement (pixel) as a specific interface. For all of the pixels which pass the conditions of any filter, the correlated coloured pixel is overlaid on the base image. The previously mentioned passing conditions, which are the structure of each filter, are given in Table 3.1.

UHMW-*sample* interface	Filter colour	Filter condition(s)
Metal	Red	$E(t)^{max} > 0.1$ (arb. units)
Air	Yellow	$\Delta t_{p-p} \leqslant -1.75$ ps
Water	Blue	$\Delta t_{p-p} \geqslant 2.20$ ps
		$\int_{0.377\,\mathrm{THz}}^{0.628\,\mathrm{THz}} \lvert\tilde{E}(\omega)\rvert d\omega \leqslant 2.25$ (arb. units)
		$-8.0 \leqslant \phi_o \leqslant -5.4$ (rads)
Glass	Green	$0.06 \leqslant E(t)^{max} \leqslant 0.09$ (arb. units)
		$-0.0551 \leqslant E(t)^{min} \leqslant -0.0400$ (arb. units)
		$-0.20 \leqslant \phi_o \leqslant 0.20$ (rads)

Table 3.1: The passing conditions for each interface-specific image filter. For any pixel which pass *all* conditions of *any* filter, that pixel assumes the filter colour and overlays the base spatial image of the concealed interfaces.

The set of measurements contained by the reflection image data is analyzed by the image filters specifically outlined in Table 3.1, and the resulting overlays are individually applied to the base amplitude image (integrated from 0.377 THz to 0.628 THz). The resulting spatial images from each filter are presented in Figure 3.22.

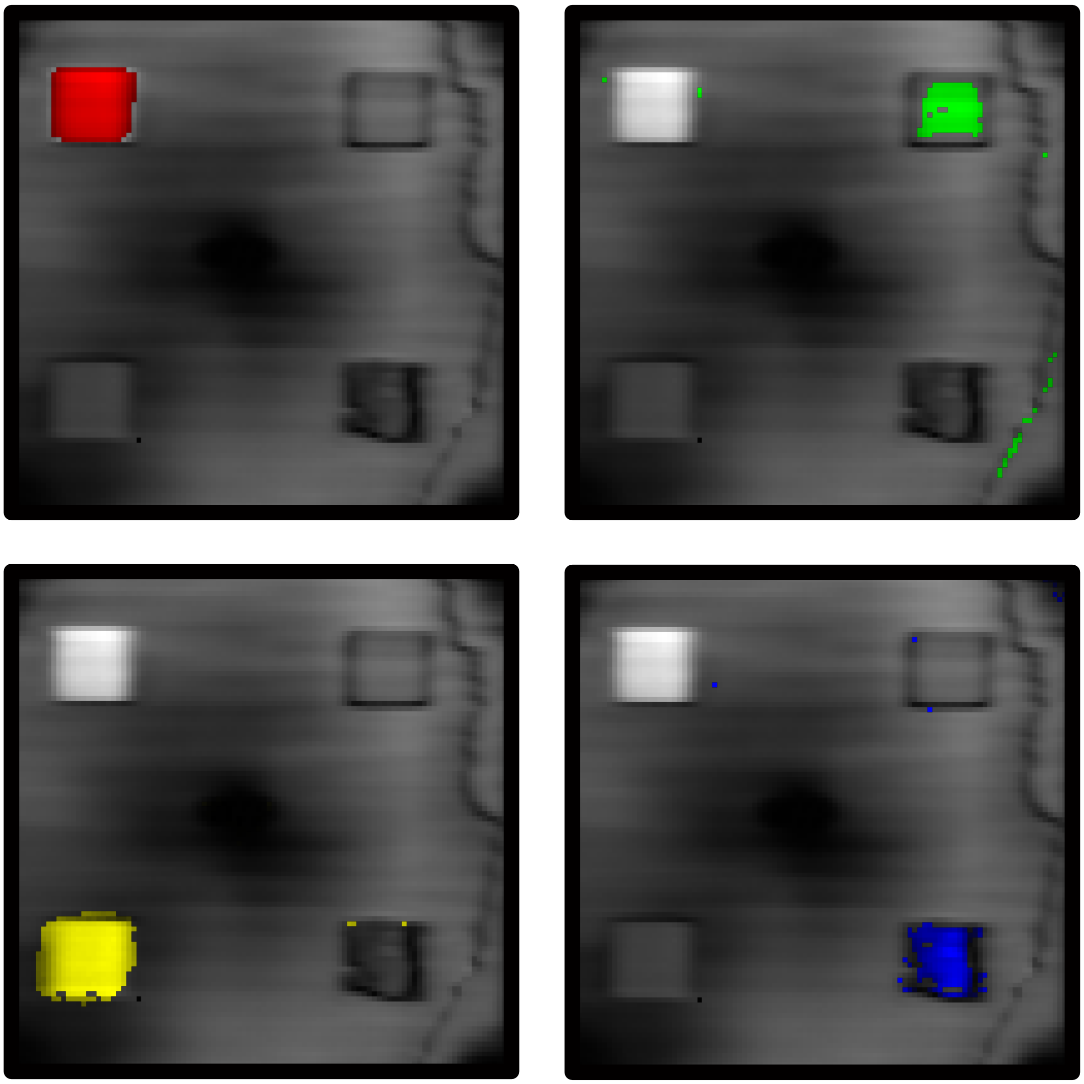

Figure 3.22: Each concealed interface filter applied to the spatial image of the electric field amplitude, integrated from 0.377 THz to 0.628 THz, identifying UHMW-metal (red), UHMW-glass (green), UHMW-air (yellow), and UHMW-water (blue) interfaces.

Chapter 4

Discussion and Future Work

4.1 Summary

The main results obtained in Chapter 3 demonstrate the clear distinction between different concealed interfaces within a layered, insulated system by means of a 100 by 100 spatial THz reflection image in conjunction with a filtering technique for the identification of the interface materials. Initially, transmission spectroscopy of UHMW and glass is performed which extracts the index of refraction of each material, confirms the applicability of UHMW as the insulating layer of the imaging sample, and validates the developed reflection spectroscopy technique. The implementation of dove prism reflection spectroscopy allows for the convenient testing of different interfaces, and illustrates the contrasts among reflections from the interfaces. It also allows the choice of the most sensitive polarization configuration. Following the collection of the concealed interface image data, the amplitude and phase images display key differences between some interfaces. In order to generate the interface-specific filters, numerous amplitude and phase features of the reflected electric fields are analyzed and categorized with respect to each UHMW-sample interface. The construction of each interface-specific image filter relies on the visual comparison of these quantified electric field traits of reflected THz pulses by developing spatial images from these calculated values. In each image generated from a THz pulse trait, observations are made suggesting the distinguishability of one interface from the remaining interfaces. Identification conditions, based on the quantification of the pulsed electric field characteristics, are established for each interface, and they are applied to the collection of measurements composing the reflection image to successfully identify regions of each concealed interface investigated in this thesis.

4.2 Discussion of the Key Results

The application of each interface-specific image filter yields four 100 by 100 images of the spatial locations of all interfaces with coloured pixels overlaying the corresponding region containing the successfully identified concealed interface. Each concealed interface (UHMW-metal, UHMW-glass, UHMW-air, and UHMW-water) is spatially identified within the imaging sample (even with multiple sources of noise in specific areas of the imaging sample) by its indicated colour.

The identification of the UHMW-metal and UHMW-air interfaces makes use of a single filter condition. From the large reflectance of polished metal, the trait that discriminates the metal interface from the rest is the large reflected electric field amplitude. This is sufficient to successfully identify the region of metal throughout the entire imaging sample.

Due to the decrease in refractive index from UHMW to air, this interface reflects incident electric fields internally, rather than externally, introducing an expected relative π phase shift with respect to the other interfaces. This phase shift is identified by the characteristic time-width of the THz pulse from peak-to-peak Δt_{p-p}. Since these values are calculated by the difference of the time delays of the maximum and minimum peaks, the π phase shifted UHMW-air reflection gives a large negative value for the time-width, as opposed to positive values for the other interfaces. The UHMW-air interface is also identified by Δt_{p-p} throughout the noise given by small air gaps within the expected UHMW-UHMW interfaces (which often consist of small air gaps, i.e. less uniform UHMW-air interfaces). The reflections from these unwanted interfaces reflect with the same phase shift, however due to the non-uniformity and small size of the air gaps, the reflected electric field is lesser in amplitude, thus Δt_{p-p} is smaller in magnitude. As it turns out, the characteristic peak-to-peak time-width Δt_{p-p} identifies and substantially diminishes the noise introduced by unwanted air gaps within the entire image, for all concealed interfaces. Collectively, the unique phase shift and relatively large amplitude of the concealed UHMW-air interface allow for its identification.

The identification of UHMW-water and UHMW-glass interfaces is more convoluted, in comparison, each consisting of three unique conditions to be satisfied to map out the respective image filter. The detection of water within the layered system is based on a lesser amplitude within the amplitude image integrated over a small range of frequencies, as well as a unique range among the values of the initial phase offset ϕ_o. The UHMW-glass interface is similarly identified, by specifying ranges of values for the amplitudes of the minimum and maximum peaks, as well as the phase offset.

The incorrect identification of some pixels among the spatial image must be addressed. Due to the significant distinction between the reflecting amplitude from the UHMW-metal interface and others, there are no pixels misidentified as a UHMW-metal interface. For the other interfaces, however, some pixels near the far right edge of the image or the borders of a region are improperly identified. The locations of the misidentified pixels are not surprising since at these edges or borders, it is expected that THz pulses are reflecting from two interfaces, simultaneously. For example, if the pulses are aligned such that half of the pulse is incident on a UHMW-air interface, and the other half is incident on a UHMW-metal interface, then the detected reflection is a superposition of the two reflected electric fields. In this case, the two reflections are out-of-phase, so the resulting reflection may appear to be a single reflection from a different interface.

It is assumed that a similar effect is dominant on the far right of the images, for example, at the edge of the imaging sample, a portion of the pulse may have reached the reflecting interface of the imaging sample from its side, without initially refracting through the top layer of the sample. This essentially clips the detected THz pulse, reflecting with a lesser amplitude, leading to its misidentification.

Known sources of noise are also recognized at the center and corners of the images. At these locations, the imaging sample is bolted to the translation stage. In these regions, the noise floor of the THz-TDS system is detected, thus creating a dark region in amplitude images and leading to extreme values for the determination of the phase. Nonetheless, these regions do not interfere with the imaging and identification of concealed interfaces.

The temperature-dependence of the time delay of a THz pulse may have been observed in the phase image selected at 0.251 THz. On the right side of the image, the average phase value between the UHMW-glass and UHMW-water interfaces is noticeably inconsistent with that on the left side of the image. It is noted that temperature fluctuations may cause internal drift of the extracted time delay of a THz pulse. Since the phase of an electric field is extremely sensitive to changes in time delay, the effects of temperature fluctuations have surfaced after generating the phase image. It seems that along a given vertical line in the image, the phase values are rather consistent (or gradually changing), as opposed to the sudden shifts in phase values along a horizontal line. This horizontal sectioning of phase values also supports the above conclusion since from the nature of the raster scan in this thesis, the y-axis is traversed much more frequently than the x-axis, thus the phase fluctuations caused by long-term temperature shifts are more pronounced along the x-axis.

Another possible source of the sudden transition in phase of the reflected electric fields on the right side of the image is the design of the instrument used to block the front reflection at the top surface of the imaging sample. Since this thin metal object is fixed directly above the imaging sample, along the y-axis, as the imaging sample is translated along the x-axis, any small changes in thickness or height of the imaging sample introduce a small gap between the front reflection blocker and the surface of the sample. Therefore in some regions, a portion of the unwanted reflected THz pulse at the top surface of the imaging sample may have been detected, in superposition with the reflection of interest from the concealed interfaces, which affects the calculated phase.

4.3 Future Work

In the THz reflection imaging experiment, a 100 by 100 set of reflection measurements, selected for the depth of the concealed interfaces, are collected with the use of a THz-TDS system. By averaging 1000 waveforms per measurement, and pausing reflection collection over the duration of sample translation between measurements, the image data acquisition lasts approximately 12 hours for a single 100 by 100 image.

The next logical step would be to repeat the experiments for the TM configuration, which is shown in Section 3.3, to potentially demonstrate a higher degree of contrast between the concealed materials. This is also necessary to refine the coloured filters based on considerations of physical theory. There are also many variables that can be adjusted to maximize the efficiency of the imaging system for the purpose of concealed interface identification, now that the concept has been demonstrated successfully. This may involve averaging over fewer waveforms or reducing the resolution of the collected image data, as appropriate for a given industrial setting in order to test these principles for a specific application.

The duration of the image data collection also has an impact on the consistency of the reflection measurements since temperature fluctuations in the THz-TDS system, introduce a small time delay drift in the measurements. The greater the duration is of the imaging process, the greater the likelihood is of temperature impacting the measured time delay of a THz pulse. This is observed in the phase images since the calculated phase is extremely sensitive to the delay, thus sensitive to the drift.

In order to accurately determine the phase data, the reliability of the front reflection blocker, used to prevent detection of the THz pulses reflected from the top surface of the imaging sample, must be ensured. The stationary mounting of a thin metal piece directly above the sample works for a perfectly flat and uniformly thick sample, however in practice, this may not be a realistic approximation. As the thickness changes, the distance between the blocker and the surface of the sample also changes. In order to fully prevent front reflections from being detected, a simple adjustment can be made, such as a constant force supplied downwards against the reflection blocker while restricting its motion along the z-axis (up and down).

By exploring the implementation of other materials, as opposed to UHMW, as the insulating material in the layered system, a different range of identifiable interfaces may arise, assuming that the identification of an interface among other materials can be based on the contrast in dielectric features. A steep change in refractive index of the insulating medium may significantly alter the possibility of identifying interfaces composed of materials with a low index of refraction.

With the success of identifying each interface within the layered system with minimal false identifications, this experiment can be repeated with a more diverse and larger selection of concealed interfaces. In this revised experiment, a focus may be drawn on discovering the required limit of contrast (or difference) between the dielectric properties of two materials in order to identify the interfaces formed in the imaging sample. Since the UHMW-metal interface is simply identifiable, a deeper look at metallic interfaces may be undertaken. Remaining in the realm of applications related to identifying indicators of corrosion before it takes place, various samples of painted and corroded metal can be imaged to test the distinguishability between the respective UHMW-sample interfaces within the layered system. Referring to the work of Anastasi and Madaras [26], the ability to detect corrosion under painted surfaces with THz reflection imaging is available by the determination of surface roughness and response to paint thickness. By inspecting rough, corroded or painted metals within the layered system, identification of these differences among other interfaces, along with precursors of corrosion, may be possible.

4.4 Conclusion

The experiment and techniques performed within this thesis have validated the feasibility of conducting THz reflection imaging to spatially map the structure of concealed interfaces at a given depth, while simultaneously identifying each interface material without the use of a reference beam, commonly required for reflection spectroscopy. The specific involvement of water and metal, among other interfaces, demonstrates the applicability of this technique for the detection of pre-corrosion within a practical system. Initially, the employment of THz transmission spectroscopy establishes UHMW as a suitable coating in a system probed by radiation at these frequencies. The subsequent development of a dove prism reflection spectroscopy system aids in understanding THz reflections at different interfaces and realizing contrasting reflections for different materials, thus identifying materials likely to be distinguished in a layered UHMW system. Concealed interfaces are then imaged with the construction of a reflection imaging system using TE polarization. Guided by the results from dove prism reflection spectroscopy, numerous pulsed electric field characteristics from the image measurements are investigated, and interface-specific filters are developed. Applying these filters produces a colourmap of the interface materials, overlaying the spatial image. The spatial location and identification of each interface material is performed with minimal false identifications. The filtered images demonstrate the ability to apply reflection spectroscopy techniques to a practical, insulated, system to spatially map and identify various concealed interfaces (without using a reference measurement) based on electric field amplitude and phase properties (despite the sensitivity of phase to minuscule changes in position or thickness), including the detection of water among other metallic and dielectric materials. The identification of water (and other dielectric materials) in this manner suggests further exploration of this method towards a variety of relevant industrial applications for the purpose of identifying precursors to the corrosion of a protected, insulated structure, which may significantly impact the cost, duration, and intricacies of repair.

Bibliography

[1] D. M. Mittleman, R. H. Jacobsen, and M. C. Nuss, "T-ray imaging," *IEEE Journal on Selected Topics in Quantum Electronics*, vol. 2, no. 3, pp. 679–692, 1996.

[2] D. Mittleman, *Sensing with Terahertz Radiation*, ser. Springer Series in Optical Sciences. Springer-Verlag Berlin Heidelberg, 2003.

[3] R. Köhler, A. Tredicucci, F. Beltram, H. E. Beere, E. H. Linfield, A. G. Davies, D. A. Ritchie, R. C. Iotti, and F. Rossi, "Terahertz semiconductor-heterostructure laser," *Nature*, vol. 417, no. 6885, pp. 156–159, 2002.

[4] X. Shen, C. R. Dietlein, E. Grossman, Z. Popovic, and F. G. Meyer, "Detection and segmentation of concealed objects in terahertz images," *IEEE Transactions on Image Processing*, vol. 17, no. 12, pp. 2465–2475, 2008.

[5] L. Afsah-Hejri, P. Hajeb, P. Ara, and R. J. Ehsani, "A Comprehensive Review on Food Applications of Terahertz Spectroscopy and Imaging," *Comprehensive Reviews in Food Science and Food Safety*, vol. 18, no. 5, pp. 1563–1621, 2019.

[6] J. F. Federici, B. Schulkin, F. Huang, D. Gary, R. Barat, F. Oliveira, and D. Zimdars, "THz imaging and sensing for security applications—explosives, weapons and drugs," *Semiconductor Science and Technology*, vol. 20, no. 7, pp. S266–S280, 2005.

[7] K. Fukunaga and M. Picollo, "Terahertz spectroscopy applied to the analysis of artists' materials," *Applied Physics A: Materials Science and Processing*, vol. 100, no. 3, pp. 591–597, 2010.

[8] P. H. Siegel, "Terahertz technology in biology and medicine," *IEEE Transactions on Microwave Theory and Techniques*, vol. 52, no. 10, pp. 2438–2447, 2004.

[9] J. Takayanagi, H. Jinno, S. Ichino, K. Suizu, M. Yamashita, T. Ouchi, S. Kasai, H. Ohtake, H. Uchida, N. Nishizawa, and K. Kawase, "High-resolution time-of-flight terahertz tomography using a femtosecond fiber laser," *Optics Express*, vol. 17, no. 9, p. 7533, 2009.

[10] A. Redo-Sanchez, N. Laman, B. Schulkin, and T. Tongue, "Review of Terahertz Technology Readiness Assessment and Applications," *Journal of Infrared, Millimeter, and Terahertz Waves*, vol. 34, no. 9, pp. 500–518, 2013.

[11] M. C. Kemp, P. F. Taday, B. E. Cole, J. A. Cluff, A. J. Fitzgerald, and W. R. Tribe, "Security applications of terahertz technology," in *Terahertz for Military and Security Applications*, R. J. Hwu and D. L. Woolard, Eds., vol. 5070. SPIE, 2003, p. 44.

[12] S. Hadjiloucas, L. S. Karatzas, and J. W. Bowen, "Measurements of leaf water content using terahertz radiation," *IEEE Transactions on Microwave Theory and Techniques*, vol. 47, no. 2, pp. 142–149, 1999.

[13] M. van Exter, C. Fattinger, and D. Grischkowsky, "Terahertz time-domain spectroscopy of water vapor," *Optics Letters*, vol. 14, no. 20, p. 1128, 1989.

[14] T. Kleine-Ostmann, T. Knobloch, M. Koch, S. Hoffmann, M. Breede, M. Hofmann, G. Hein, K. Pierz, M. Sperling, and K. Donhuijsen, "Continuous-wave THz imaging," *Electronics Letters*, vol. 37, no. 24, pp. 1461–1463, 2001.

[15] M. C. Nuss and J. Orenstein, "Terahertz time-domain spectroscopy," in *Millimeter and Submillimeter Wave Spectroscopy of Solids*. Springer Berlin Heidelberg, 1998, pp. 7–50.

[16] T. Bowman, T. Chavez, K. Khan, A. Chakraborty, J. Wu, K. Bailey, and M. El-Shenawee, "Statistical signal processing for quantitative assessment of pulsed terahertz imaging of human breast tumors," in *International Conference on Infrared, Millimeter, and Terahertz Waves, IRMMW-THz*. IEEE Computer Society, 2017.

[17] C. Jördens and M. Koch, "Detection of foreign bodies in chocolate with pulsed terahertz spectroscopy," *Optical Engineering*, vol. 47, no. 3, p. 037003, 2008.

[18] M. C. Kemp, "Explosives detection by terahertz spectroscopy - A bridge too far?" *IEEE Transactions on Terahertz Science and Technology*, vol. 1, no. 1, pp. 282–292, 2011.

[19] P. Kilcullen, M. Shegelski, M. Na, D. Purschke, F. Hegmann, and M. Reid, "Terahertz Spectroscopy and Brewster Angle Reflection Imaging of Acoustic Tiles," *Journal of Spectroscopy*, vol. 2017, 2017.

[20] R. F. Anastasi, E. I. Madaras, J. P. Seebo, S. W. Smith, J. K. Lomness, P. E. Hintze, C. C. Kammerer, W. P. Winfree, and R. W. Russell, "Terahertz NDE application for corrosion detection and evaluation under Shuttle tiles," in *Nondestructive Characterization for Composite Materials, Aerospace Engineering, Civil Infrastructure, and Homeland Security 2007*, vol. 6531. SPIE, 2007, p. 65310W.

[21] C. Rønne, P. O. Åstrand, and S. R. Keiding, "THz spectroscopy of liquid H2O and D2O," *Physical Review Letters*, vol. 82, no. 14, pp. 2888–2891, 1999.

[22] B. B. Hu and M. C. Nuss, "Imaging with terahertz waves," *Optics Letters*, vol. 20, no. 16, p. 1716, 1995.

[23] K. Kawase, Y. Ogawa, Y. Watanabe, and H. Inoue, "Non-destructive terahertz imaging of illicit drugs using spectral fingerprints," *Optics Express*, vol. 11, no. 20, p. 2549, 2003.

[24] Y. C. Shen, T. Lo, P. F. Taday, B. E. Cole, W. R. Tribe, and M. C. Kemp, "Detection and identification of explosives using terahertz pulsed spectroscopic imaging," *Applied Physics Letters*, vol. 86, no. 24, p. 241116, 2005.

[25] D. M. Mittleman, R. H. Jacobsen, R. Neelamani, R. G. Baraniuk, and M. C. Nuss, "Gas sensing using terahertz time-domain spectroscopy," *Applied Physics B: Lasers and Optics*, vol. 67, no. 3, pp. 379–390, 1998.

[26] R. F. Anastasi and E. I. Madaras, "Terahertz NDE for under paint corrosion detection and evaluation," in *AIP Conference Proceedings*, vol. 820 I, 2006, pp. 515–522.

[27] C. Stoik, M. Bohn, and J. Blackshire, "Nondestructive evaluation of aircraft composites using reflective terahertz time domain spectroscopy," *NDT and E International*, vol. 43, no. 2, pp. 106–115, 2010.

[28] D. Grischkowsky, S. Keiding, M. van Exter, and C. Fattinger, "Far-infrared time-domain spectroscopy with terahertz beams of dielectrics and semiconductors," *Journal of the Optical Society of America B*, vol. 7, no. 10, p. 2006, 1990.

[29] A. D. Burnett, J. E. Cunningham, A. G. Davies, P. Dean, and E. H. Linfield, "Terahertz frequency spectroscopy and its potential for security applications," *Infrared and Raman Spectroscopy in Forensic Science*, pp. 295–314, 2012.

[30] L. Thrane, R. H. Jacobsen, P. Uhd Jepsen, and S. R. Keiding, "THz reflection spectroscopy of liquid water," *Chemical Physics Letters*, vol. 240, no. 4, pp. 330–333, 1995.

[31] P. Uhd Jepsen and B. M. Fischer, "Dynamic range in terahertz time-domain transmission and reflection spectroscopy," *Optics Letters*, vol. 30, no. 1, p. 29, 2005.

[32] K. Sakai *et al.*, *Terahertz optoelectronics*, ser. Topics in Applied Physics. Springer-Verlag Berlin Heidelberg, 2005, vol. 6.

[33] A. G. Davies, E. H. Linfield, and M. B. Johnston, "The development of terahertz sources and their applications," *Phys. Med. Biol.*, vol. 47, no. 21, pp. 3679–3689, 2002.

[34] L. Xu, X. C. Zhang, and D. H. Auston, "Terahertz beam generation by femtosecond optical pulses in electro-optic materials," *Applied Physics Letters*, vol. 61, no. 15, pp. 1784–1786, 1992.

[35] L. Duvillaret, F. Garet, and J.-L. Coutaz, "Highly precise determination of optical constants and sample thickness in terahertz time-domain spectroscopy," *Applied Optics*, vol. 38, no. 2, p. 409, 1999.

[36] G. Mourou, C. V. Stancampiano, A. Antonetti, and A. Orszag, "Picosecond microwave pulses generated with a subpicosecond laser-driven semiconductor switch," *Applied Physics Letters*, vol. 39, no. 4, pp. 295–296, 1981.

[37] D. H. Auston, K. P. Cheung, and P. R. Smith, "Picosecond photoconducting Hertzian dipoles," *Applied Physics Letters*, vol. 45, no. 3, pp. 284–286, 1984.

[38] P. R. Smith, D. H. Auston, and M. C. Nuss, "Subpicosecond Photoconducting Dipole Antennas," *IEEE Journal of Quantum Electronics*, vol. 24, no. 2, pp. 255–260, 1988.

[39] P. Uhd Jepsen, C. Winnewisser, M. Schall, and V. Schyja, "Detection of THz pulses by phase retardation in lithium tantalate," *Physical Review E - Statistical Physics, Plasmas, Fluids, and Related Interdisciplinary Topics*, vol. 53, no. 4, pp. R3052–R3054, 1996.

[40] A. Nahata, A. S. Weling, and T. F. Heinz, "A wideband coherent terahertz spectroscopy system using optical rectification and electro-optic sampling," *Applied Physics Letters*, vol. 69, no. 16, pp. 2321–2323, 1996.

[41] N. M. Burford and M. O. El-Shenawee, "Review of terahertz photoconductive antenna technology," *Optical Engineering*, vol. 56, no. 1, p. 010901, 2017.

[42] Z. Piao, M. Tani, and K. Sakai, "Carrier dynamics and terahertz radiation in photoconductive antennas," *Japanese Journal of Applied Physics, Part 1: Regular Papers and Short Notes and Review Papers*, vol. 39, no. 1, pp. 96–100, 2000.

[43] P. Chen, M. Hosseini, and A. Babakhani, "An integrated germanium-based THz impulse radiator with an optical waveguide coupled photoconductive switch in silicon," *Micromachines*, vol. 10, no. 6, 2019.

[44] C. M. Collier, B. Born, M. Bethune-Waddell, X. Jin, and J. F. Holzman, "Ultrafast photoexcitation and transient mobility of GaP for photoconductive terahertz emission," *IEEE Journal of Quantum Electronics*, vol. 49, no. 8, pp. 691–696, 2013.

[45] C. M. Collier, T. J. Stirling, I. R. Hristovski, J. D. Krupa, and J. F. Holzman, "Photoconductive terahertz generation from textured semiconductor materials," *Scientific Reports*, vol. 6, no. 1, pp. 1–10, 2016.

[46] M. Naftaly, A. P. Foulds, R. E. Miles, and A. G. Davies, "Terahertz transmission spectroscopy of nonpolar materials and relationship with composition and properties," *International Journal of Infrared and Millimeter Waves*, vol. 26, no. 1, pp. 55–64, 2005.

[47] M. Hangyo, T. Nagashima, and S. Nashima, “Spectroscopy by pulsed terahertz radiation,” *Measurement Science and Technology*, vol. 13, no. 11, p. 1727, 2002.

[48] V. P. Wallace, E. MacPherson, J. A. Zeitler, and C. Reid, “Three-dimensional imaging of optically opaque materials using nonionizing terahertz radiation,” *Journal of the Optical Society of America A*, vol. 25, no. 12, p. 3120, 2008.

[49] D. Griffiths, *Introduction to Electrodynamics*. Upper Saddle River, N.J., Prentice Hall, 1999.

[50] I. Pupeza, R. Wilk, and M. Koch, “Highly accurate optical material parameter determination with THz time-domain spectroscopy,” *Optics Express*, vol. 15, no. 7, p. 4335, 2007.

[51] L. Duvillaret, F. Garet, and J. L. Coutaz, “A reliable method for extraction of material parameters in terahertz time-domain spectroscopy,” *IEEE Journal on Selected Topics in Quantum Electronics*, vol. 2, no. 3, pp. 739–745, 1996.

[52] X. Li, Z. Hong, J. He, and Y. Chen, “Precisely optical material parameter determination by time domain waveform rebuilding with THz time-domain spectroscopy,” *Optics Communications*, vol. 283, no. 23, pp. 4701–4706, 2010.

[53] Advanced Photonix Inc., “T-Ray 5000,” Accessed: 29 April 2020. [Online]. Available: https://www.advancedphotonix.com/thz/products/t-ray5000

[54] L. C. Wang, M. K. Harvey, J. C. Ng, and U. Scheunemann, “Ultra-high molecular weight polyethylene (UHMW-PE) and its application in microporous separators for lead/acid batteries,” *Journal of Power Sources*, vol. 73, no. 1, pp. 74–77, 1998.

[55] L. E. Govaert and P. J. Lemstra, “Deformation behavior of oriented UHMW-PE fibers,” *Colloid & Polymer Science*, vol. 270, no. 5, pp. 455–464, 1992.

[56] J. Dai, J. Zhang, W. Zhang, and D. Grischkowsky, “Terahertz time-domain spectroscopy characterization of the far-infrared absorption and index of refraction of high-resistivity, float-zone silicon,” *Journal of the Optical Society of America B*, vol. 21, no. 7, p. 1379, 2004.

[57] A. K. Cherri and M. S. Alam, “Accurate measurement of small Gaussian laser beam diameters using various rulings,” *Optics Communications*, vol. 223, no. 4-6, pp. 255–262, 2003.

[58] MathWorks Inc., “Fast Fourier transform - MATLAB,” Accessed: 15 May 2020. [Online]. Available: https://www.mathworks.com/help/matlab/ref/fft.html

[59] P. Uhd Jepsen, U. Møller, and H. Merbold, "Investigation of aqueous alcohol and sugar solutions with reflection terahertz time-domain spectroscopy," *Optics Express*, vol. 15, no. 22, p. 14717, 2007.

[60] E. J. Zeman and G. C. Schatz, "An accurate electromagnetic theory study of surface enhancement factors for silver, gold, copper, lithium, sodium, aluminum, gallium, indium, zinc, and cadmium," *The Journal of Physical Chemistry*, vol. 91, no. 3, pp. 634–643, 1987.

[61] ThorLabs Inc., "Protected Silver Mirrors," Accessed: 7 June 2020. [Online]. Available: https://www.thorlabs.com

[62] A. Wojdyla and G. Gallot, "Brewster's angle silicon wafer terahertz linear polarizer," *Optics Express*, vol. 19, no. 15, p. 14099, 2011.

[63] J. Xu, K. W. Plaxco, and S. J. Allen, "Absorption spectra of liquid water and aqueous buffers between 0.3 and 3. 72 THz," *Journal of Chemical Physics*, vol. 124, no. 3, p. 036101, 2006.

[64] T. Hattori, H. Kumon, and H. Tamazumi, "Terahertz spectroscopic characterization of paper," in *IRMMW-THz 2010 - 35th International Conference on Infrared, Millimeter, and Terahertz Waves, Conference Guide*, 2010.